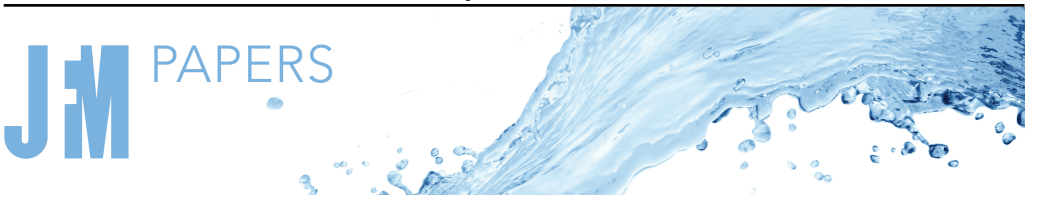
J. Fluid Mech. (2026), *vol.* 1035, A18, doi:10.1017/jfm.2026.11553



Causal analysis of a turbulent shear flow model

Yongyi Wang[1,2,3], **Jiaqing Kou**[1,2,3], **Bernd R. Noack**[4,5] **and Weiwei Zhang**[1,2,3]

[1]School of Aeronautics, Northwestern Polytechnical University, Xi'an 710072, PR China

[2]International Joint Institute of Artificial Intelligence on Fluid Mechanics, Northwestern Polytechnical University, Xi'an 710072, PR China

[3]National Key Laboratory of Aircraft Configuration Design, Xi'an 710072, PR China

[4]School of Mechatronics and Control Engineering, Shenzhen University, Canghai campus, Shenzhen 518060, PR China

[5]Guangdong Province VTOL Aircraft Manufacturing Innovation Center, Shenzhen 518060, PR China

Corresponding author: Jiaqing Kou, jqkou@nwpu.edu.cn

(Received 27 September 2025; revised 19 March 2026; accepted 11 April 2026)

We perform causal analysis on the low-dimensional Galerkin model for shear flow developed by Moehlis *et al.* (*New J. Phys.*, vol. 6, 2004, 56). Our method integrates both equation-based analysis and the proposed Galerkin-based Granger causality (GGC) to investigate the effect of the nonlinear terms on the dynamics. Two types of quadratic interactions are identified: a fully triadic interaction and a modulated two-mode coupling. The propagation of these interactions through the nonlinear dynamics leads to a directed cause-and-effect network. Furthermore, the relative importance of each mode amplitude on the dynamics of the target mode is quantified. This analysis provides a deeper understanding of the nonlinear dynamics and distills control opportunities. To demonstrate the applicability of the proposed GGC to realistic flows where Galerkin projection is impractical, a turbulent lid-driven cavity flow is further studied. We foresee applications of the proposed causal analysis framework as valuable tools for Galerkin modelling – guiding investigations of modal causality, prediction uncertainty, model-order reduction and control design.

Key words: nonlinear dynamical systems, low-dimensional models, flow control

1. Introduction

Discovering causality has long been the central focus of scientific research (Camps-Valls *et al.* 2023; Martínez-Sánchez *et al.* 2024). Despite rich data from experiments and simulations, extracting cause-and-effect relationships from complex flow phenomena remains a challenging task (Lozano-Durán *et al.* 2020; Lozano-Durán & Arranz 2022).

© The Author(s), 2026. Published by Cambridge University Press.

https://doi.org/10.1017/jfm.2026.11553 Published online by Cambridge University Press

Randomised controlled trials, the gold standard for causal analysis, are often infeasible in such systems. This underscores the need for efficient causal inference of complex flows. To this end, data-driven causal analysis emerges as a promising solution, where causality is identified by detecting information transfer within a large amount of data. To illustrate this, consider variable p as the cause of variable q. It can be posited that specific information must initially appear in variable p and subsequently be transmitted to variable q. Various algorithms have been developed to quantify the transfer of information between variables. Typical methods include Granger causality in economics (Granger 1969), which defines causality as the contribution of one variable to the prediction of another. Effective information (Tononi & Sporns 2003), a concept from network science, quantifies causality as the difference between determinism and degeneracy within a dynamical system. Transfer entropy (Schreiber 2000) is a nonlinear causal inference method that uses Shannon entropy to measure the uncertainty between variables. If the presence of variable p diminishes the uncertainty of variable q, a causal relationship is indicated from p to q.

Data-driven causal analysis has the potential to offer valuable solutions to a range of challenging problems in the field of fluid dynamics. Tissot *et al.* (2014) utilised Granger causality to examine the causal relationships between the various velocity components in the logarithmic layer of wall turbulence. Their findings indicated that streak breakdowns initiate jets that are perpendicular to the wall surface. Lozano-Durán *et al.* (2020) applied transfer entropy to examine causalities between energy-containing eddies, revealing similar causal patterns between the buffer layer and the logarithmic layer. Lozano-Durán *et al.* (2021) studied the impact of modifying linear terms by introducing controls into self-sustaining wall turbulence, revealing the mechanism of linear energy transfer from mean flow to fluctuating velocities. These studies provide useful information for understanding wall turbulence from the perspective of causality. In a study of isotropic turbulence, Jiménez (2018) successfully identified regions of importance by applying perturbations to a specific area and observing the resulting effects. This method was applied to two-dimensional isotropic turbulence (Jiménez 2018) and three-dimensional isotropic turbulence (Encinar & Jiménez 2023). Causal analysis also facilitates the understanding of fluid–structure Interaction phenomena. Zhang *et al.* (2018) revealed the causal relationship between tandem wings in uniform airflow using transfer entropy. Bagchi, Unni & Saha (2023) analysed the relationship between structural oscillation and Reynolds number in jet-induced vibrations of a cantilever beam using Pearson correlation and Granger causality. Wang *et al.* (2021, 2022) investigated boundary-layer–porous-media interactions using transfer entropy, revealing how permeability affects the intensity, time scale and spatial extent of these interactions. Furthermore, causal analysis has been used to investigate the association between pressure fluctuation at various locations within a jet (Omata & Tsutsumi 2020) to identify the regions from which aerodynamic noise originates. Martínez-Sánchez *et al.* (2024) decompose causalities into synergistic, unique and redundant components (SURD), revealing a top-down causal effect from outer-layer velocity to the inner layer in wall turbulence. Their follow-up study (Martínez-Sánchez & Lozano-Durán 2025) further demonstrates that causality can be state-dependent, and proposes a state-aware SURD framework applicable to such scenarios. We also note that modern explainability tools (e.g. SHAP) have been applied to identify dynamically influential regions in complex turbulent flows (Cremades *et al.* 2024, 2025). While not a formal inference in the Granger or Pearl sense, SHAP is implicitly grounded in a counterfactual reasoning framework, thereby offering a causally inspired perspective for interpreting black-box models.

https://doi.org/10.1017/jfm.2026.11553 Published online by Cambridge University Press

Due to the high dimensionality of complex flows, direct causal analysis on flow data is nearly infeasible. As an alternative, causal analysis on reduced-order models (ROMs) is a more practical way, which has been supported by several works (Tissot *et al.* 2014; Martínez-Sánchez *et al.* 2023). Such ROMs represent complex flow systems with low-dimensional manifolds, enabling efficient analysis, prediction and flow control (Galletti *et al.* 2004; Akhtar 2008; Rigas *et al.* 2014; Guastoni *et al.* 2021). Various ROMs have been developed, for example: (i) proper orthogonal decomposition (POD) (Lumley 1967; Sirovich 1987; Towne, Schmidt & Colonius 2018; Mendez, Balabane & Buchlin 2019), which decomposes flow snapshots into a series of orthogonal modes ordered by energy; (ii) dynamic mode decomposition (Rowley *et al.* 2009; Schmid 2010; Chen, Tu & Rowley 2012; Noack *et al.* 2016; Le Clainche & Vega 2017), rooted in Koopman theory, breaks down flow snapshots into a series of dynamic modes characterised by single frequencies and exponential growth rates; (iii) the Galerkin model (Deane *et al.* 1991; Holmes 2012), which provides a unique analytical perspective for dimension reduction, and after Galerkin projection, the governing equations are transformed into a set of ordinary differential equations (ODEs); and (iv) machine-learning-based ROMs (Kaiser *et al.* 2014; Brunton, Noack & Koumoutsakos 2020; Murata, Fukami & Fukagata 2020; Solera-Rico *et al.* 2024), which have emerged in recent years and are drawing growing interest from researchers.

Generally speaking, data-driven causal analysis has provided a valuable perspective, expanding our focus from individual modes to modal interactions. However, the aforementioned data-driven causal analyses have limitations. As purely data-driven approaches, they may yield computationally plausible but factually false results (Smirnov 2013; Stokes & Purdon 2017). Without sufficient prior knowledge for guidance, it is difficult to validate or interpret the obtained results. This issue is of particular concern in the field of physical research, as physical conclusions must be drawn with rigour.

In this work, we present a hybrid causal analysis framework for low-dimensional Galerkin models, through combining both equation-based analysis and the proposed Galerkin-based Granger causality (GGC). These two methods identify causality from qualitative and quantitative perspectives, respectively, and can be validated against each other. In particular, it compensates for the inherent uncertainty of data-driven methods by integrating domain knowledge. The effectiveness of this method is validated in a low-dimensional Galerkin model of turbulent shear flows, especially of the effect of nonlinear terms on the dynamics. Two types of quadratic interactions are identified, and the propagation of nonlinear terms is represented by a directed cause-and-effect network. Using the causal relationship, a causality-guided flow control is performed to demonstrate how causalities can be used in practice, where extreme events in turbulence have been successfully suppressed. To further validate the applicability of the proposed method in complex, real-world scenarios, we further analyse the causal relationship in a turbulent lid-driven cavity-flow problem.

This paper is organised as follows. Sections 2 and 3 elaborate on the theoretical foundations of the Galerkin model and classical Granger causality, respectively. In § 4, a GGC is proposed. In § 5, we apply equation-based and GGC analyses to the turbulent shear flow model proposed by Moehlis, Faisst & Eckhardt (2004). Qualitative and quantitative causal findings are provided, and a causality-guided flow control is illustrated. Finally, conclusions and perspectives are presented in § 6. The mode definition in the shear flow model and additional application of GGC on turbulent cavity flow are presented in Appendices A and B, respectively. The source codes from this research are publicly available.

https://doi.org/10.1017/jfm.2026.11553 Published online by Cambridge University Press

2. Galerkin model

The Galerkin model is one of the commonly used approaches to construct ROMs, using first principles of the Navier–Stokes equations. It projects governing equations onto spatially orthogonal modes to obtain a low-dimensional representation of flows, leading to a set of ODEs that describe the temporal evolution of mode coefficients. For example, considering the incompressible Navier–Stokes equations

$$\begin{gathered}\nabla \cdot \boldsymbol{u} = 0, \\ \frac{\partial \boldsymbol{u}}{\partial t} + (\boldsymbol{u} \cdot \nabla)\boldsymbol{u} = -\nabla p + \frac{1}{Re}\Delta \boldsymbol{u} + \boldsymbol{f}.\end{gathered} \tag{2.1}$$

where p represents pressure, and $\boldsymbol{f}$ represents body force. The velocity $\boldsymbol{u}$ is divided into two components: a constant mean flow velocity $\boldsymbol{u}_0$ and a fluctuating velocity $\boldsymbol{u}'$ that varies over time. After modal projection, the fluctuating velocity is decomposed into a linear combination of several modes. These velocity modes are mutually orthonormal, implying that the inner product of any two mode pairs is zero, i.e. $(\phi_i, \phi_j)_\Omega = 0$, $(i \neq j)$:

$$\boldsymbol{u}(t) = \boldsymbol{u}_0 + \boldsymbol{u}'(t) = \boldsymbol{u}_0 + \sum_{i=1}^{n} a_i(t)\boldsymbol{\phi}_i, \tag{2.2}$$

where n is the number of modes. The decomposed velocity is then substituted into the incompressible Navier–Stokes equations. This results in the final Galerkin model, which is a set of nonlinear ODEs of mode coefficients:

$$\frac{\mathrm{d}}{\mathrm{d}t}a_i = C_i + \frac{1}{Re}\sum_{j=1}^{n} L_{ij}a_j + \sum_{j=1}^{n}\sum_{k=1}^{n} Q_{ijk}a_j a_k. \tag{2.3}$$

The constant term in the equation arises from the pressure gradient, external body force and mean flow velocity. In incompressible flows, the inner product of the pressure gradient and the velocity mode (the first term in (2.4)) is entirely dependent on the boundary conditions (Noack, Papas & Monkewitz 2005):

$$C_i = -(\boldsymbol{\phi}_i, \nabla p)_\Omega + (\boldsymbol{\phi}_i, \boldsymbol{f})_\Omega - (\boldsymbol{\phi}_i, (\boldsymbol{u}_0 \cdot \nabla)\boldsymbol{u}_0)_\Omega + \frac{1}{Re}(\boldsymbol{\phi}_i, \Delta \boldsymbol{u}_0)_\Omega. \tag{2.4}$$

The linear term arises from viscous dissipation and the interaction between the mean flow velocity and the fluctuating velocity under convection:

$$L_{ij} = (\boldsymbol{\phi}_i, \Delta\boldsymbol{\phi}_j)_\Omega - Re((\boldsymbol{\phi}_i, (\boldsymbol{u}_0 \cdot \nabla)\boldsymbol{\phi}_j)_\Omega + (\boldsymbol{\phi}_i, (\boldsymbol{\phi}_j \cdot \nabla)\boldsymbol{u}_0)_\Omega). \tag{2.5}$$

All quadratic terms originate from nonlinear convection effects:

$$Q_{ijk} = -(\boldsymbol{\phi}_i, (\boldsymbol{\phi}_j \cdot \nabla)\boldsymbol{\phi}_k)_\Omega. \tag{2.6}$$

It is important to note that the selection of velocity modes is not without alternatives; however, it is preferable that these modes are capable of representing the primary features of the flow. Among the common approaches, projection on POD modes (Rempfer 2000; Balajewicz, Dowell & Noack 2013) and Fourier velocity modes (Waleffe 1997; Moehlis *et al.* 2004) are frequently used. In addition to projection-based techniques, an alternative pathway exists through system identification (Brunton, Proctor & Kutz 2016; Loiseau & Brunton 2018), where Galerkin equations are inferred directly from data-driven ROMs. Galerkin models offer the advantage of preserving the dominant features of unsteady flows with minimal computational cost, making them a preferable tool for studying complex flows (Rowley & Dawson 2017). However, there are several

https://doi.org/10.1017/jfm.2026.11553 Published online by Cambridge University Press

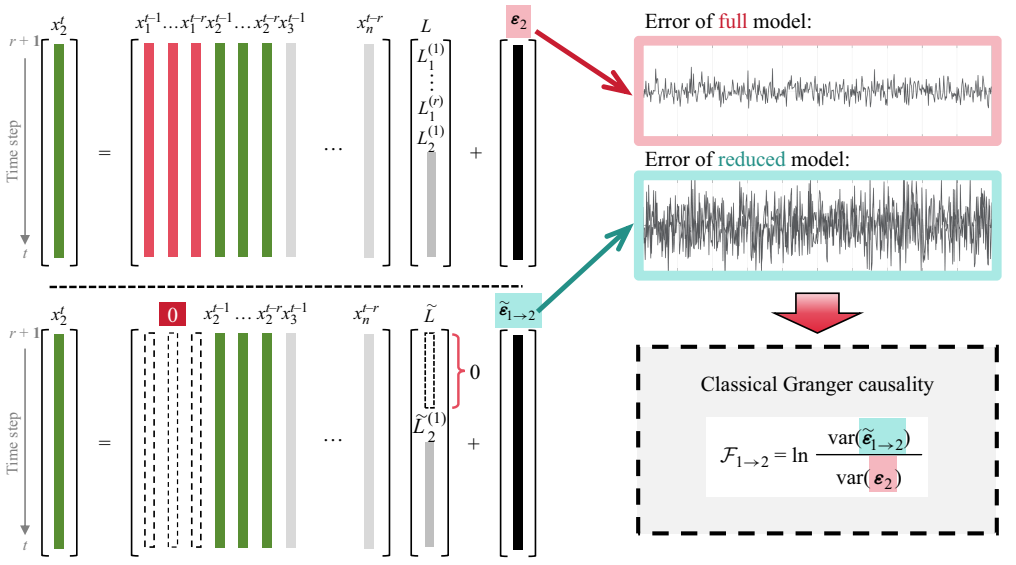


Figure 1. Schematic illustration of classical Granger causality. The computation of Granger causality from x_1 to x_2 ($\mathcal{F}_{1\to 2}$) is depicted. This measure quantifies the increase in uncertainty of x_2 when past information from x_1 is omitted, evaluated by comparing the prediction errors of the full model and the reduced model (excluding x_1 history).

drawbacks of the Galerkin models. For instance, their utilisation in compressible flows is considerably more complicated (Rowley, Colonius & Murray 2004). Galerkin models are not well suited for accommodating arbitrary domain deformations or imposing complex boundary conditions (Loiseau, Noack & Brunton 2018), and may face challenges related to stability and conservation (Iollo, Lanteri & Désidéri 2000; Balajewicz *et al.* 2013; Östh *et al.* 2014). Despite the aforementioned limitations, Galerkin models offer distinct analytical advantages that facilitate causal analysis and its validation.

3. Granger causality

In 1969, the economist Clive Granger, motivated by Wiener's theory of prediction (Wiener 1949), put forward the concept of Granger causality (Granger 1969). Since its introduction, the method has been widely applied in numerous fields that involve data analysis (Freeman 1983; Hiemstra & Jones 1994; Ding, Chen & Bressler 2006; Smirnov & Mokhov 2009). The principle of Granger causality is straightforward: if the prediction of variable q significantly deteriorates when variable p is excluded from a vector autoregressive model, then p is said to be the Granger-cause of q. A schematic illustration of classical Granger causality is shown in figure 1.

Specifically, to determine the Granger causality from x_p to x_q (denoted as $\mathcal{F}_{p\to q}$), two auto-regressive with eXogenous inputs models with a time lag of r are constructed: a full model including $\boldsymbol{x}_p$ and a reduced model excluding it. The prediction accuracy of these two models is then compared. The full model is

$$\boldsymbol{x}_q^t = \sum_{i=1}^{n}\sum_{k=1}^{r} L_i^{(k)} \boldsymbol{x}_i^{t-k} + \boldsymbol{\varepsilon}_q, \tag{3.1}$$

https://doi.org/10.1017/jfm.2026.11553 Published online by Cambridge University Press

where n denotes the total number of variables, r denotes order of time lag, $\boldsymbol{x}_q^t$ represents the time sequence of the variable q in vector, from time index $r+1$ to t, $\boldsymbol{x}_i^{t-k}$ represents the time sequence of the variable i in vector, delayed by an order of k, $L_i\boldsymbol{x}_i$ represents the linear regression term and $\boldsymbol{\varepsilon}_q$ is the model error vector. The reduced model is

$$\boldsymbol{x}_q^t = \sum_{i=1}^{n}\sum_{k=1}^{r} \tilde{L}_i^{(k)} \boldsymbol{x}_i^{t-k} + \tilde{\boldsymbol{\varepsilon}}_{p\to q} \quad (i \neq p). \tag{3.2}$$

Here, condition $i \neq p$ ensures that variable $\boldsymbol{x}_p$ is excluded from the reduced model. The tilde denotes quantities associated with the reduced model. If the exclusion of $\boldsymbol{x}_p$ impairs the prediction of $\boldsymbol{x}_q$, the variance of $\tilde{\boldsymbol{\varepsilon}}_{p\to q}$ will exceed that of $\boldsymbol{\varepsilon}_q$ from the full model. The Granger causality from $\boldsymbol{x}_p$ to $\boldsymbol{x}_q$ is then defined as the log-ratio of these two error variances:

$$\mathcal{F}_{p\to q} = \ln \frac{\mathrm{var}(\tilde{\boldsymbol{\varepsilon}}_{p\to q})}{\mathrm{var}(\boldsymbol{\varepsilon}_q)}, \tag{3.3}$$

where $\mathrm{var}(\boldsymbol{\varepsilon})$ denotes the variance of the error vector. From the perspective of information theory, Granger causality quantifies the contribution of a variable to the dynamic prediction of others; its magnitudes may have a natural interpretation in terms of information-theoretic bits per unit time (Barnett & Seth 2014). Notably, self-causalities $\mathcal{F}_{i\to i}$ are excluded from computation (appearing as zero in the maps), as Granger causality focuses on inter-variable causalities. In addition, the self-history of each mode is expected to contribute strongly to predicting its own future. Granger causality also shares conceptual similarities with sensitivity analysis (Borgonovo & Plischke 2016). Sensitivity analysis quantifies the sensitivity of outputs to variations in input parameters, i.e. typically by perturbing inputs within a defined range to assess model robustness. Granger causality specifically examines whether one time series can help predict another, thereby inferring potential causal relationships. In this sense, Granger causality can be seen as a specialised form of sensitivity analysis.

Despite its simplicity and intuitiveness, Granger causality imposes stringent definitions on its applicability. Numerous explicit or implicit assumptions serve as prerequisites for employing Granger causality (Shojaie & Fox 2022):

(i) Temporal order: causality is temporally ordered, with causes preceding effects; instantaneous causality without time delay is not considered.
(ii) Stationarity: the statistical properties of data, such as variance and mean, are time-invariant.
(iii) Linearity: the interactions between variables are assumed to be linear and can be accurately described by an autoregressive model.
(iv) Known time lag: the extent to which causality exists in the history of variables is known and is represented by a fixed time lag.
(v) Complete system: it is assumed that the analysis incorporates all relevant variables and that there are no unmeasured confounders.

These prerequisites have been designed to ensure the accuracy and reliability of Granger causality, thereby avoiding spurious causality. However, in practice, they are difficult to fully satisfy. For example, many real-world multivariate time series are non-stationary (Safikhani & Shojaie 2022); nonlinearity is a common feature in complex dynamical systems; it is also difficult to exclude all confounding factors without sufficient prior

https://doi.org/10.1017/jfm.2026.11553 Published online by Cambridge University Press

knowledge. These issues limit the application of Granger causality (Stokes & Purdon 2017), especially in fluid dynamic problems. Therefore, we introduce a GGC, a modified framework specifically developed for causal inference in Galerkin-based flow systems.

4. Galerkin-based Granger causality

The proposed GGC retains the concept and framework of classical Granger causality, while it is tailored for systems following Galerkin-structured dynamics (e.g. Navier–Stokes equations projected onto low-dimensional bases). Given that Galerkin models inherently comprise constant, linear and quadratic terms, the GGC resembles a quadratic Granger causality in form.

(i) Nonlinearity: classical Granger causality does not account for complex nonlinear interactions. Inspired by the known structure of Galerkin equations (see (2.3)), the GGC retains essential linear terms while incorporating quadratic and constant terms. This allows GGC to model nonlinear dynamics more accurately.
(ii) Relaxed stationarity assumption: complex flows are highly time-variant, where different causal relationships may emerge at different stages as the flow develops. Stationarity is relaxed in the GGC. Instead, the time-variant property is captured by a windowed analysis strategy, as detailed below.
(iii) Fixed time delay: since the Galerkin model is described by first-order ODEs, the time lag/discrete time delay in GGC is set to 1. This helps to avoid overfitting (Johansen 1988), and also eliminates possible indirect causal links.
(iv) Windowed analysis: since causalities in complex unsteady flows may vary with time, the GGC first divides the time sequence into several windows of equal length (figure 2). Within each window, the causality is computed in parallel to discover short-term causality. The ensemble average of these short-term causalities is taken to reflect the long-term causality.

The window segmentation is governed by two parameters: the window length, which denotes the length of each segment, and the window overlap, which defines the shared length between consecutive windows. In this study, the overlap is simply selected as half of the window length, whereas the window length requires careful determination as it greatly affects the final results. We observed a trade-off in window length selection: it must be sufficiently long for reliable Galerkin model estimation yet short enough to capture short-term causality. To balance these requirements, we employ the causal discriminability index (CDI) as a selection criterion, which is formally defined later in (4.5).

After the aforementioned modifications, the GGC is defined as follows. We start from a Galerkin model composed of n modes $(x_1, x_2, x_3, \cdots x_n)$. First, a suitable window length is selected to segment the time series of the mode coefficient into N equally spaced windows. To evaluate the causal effect $\mathcal{F}_{p\to q}$, a full Galerkin model is constructed that uses all modes to predict mode q in each window:

$$\boldsymbol{x}_q^t = \sum_{i=1}^{n} L_i \boldsymbol{x}_i^{t-1} + \sum_{i,j=1,i\leqslant j}^{n} Q_{ij}\boldsymbol{x}_i^{t-1}\boldsymbol{x}_j^{t-1} + C + \boldsymbol{\varepsilon}_q, \tag{4.1}$$

where $\boldsymbol{x}_q^t$ is the coefficient of mode q in vector, $L_i\boldsymbol{x}_i^{t-1}$ represents the linear terms, $Q_{ij}\boldsymbol{x}_i^{t-1}\boldsymbol{x}_j^{t-1}$ denotes the quadratic terms, both delayed by an order of 1 (one time step), C is the constant term and $\boldsymbol{\varepsilon}_q$ is the vector of prediction error. Subsequently, by

https://doi.org/10.1017/jfm.2026.11553 Published online by Cambridge University Press

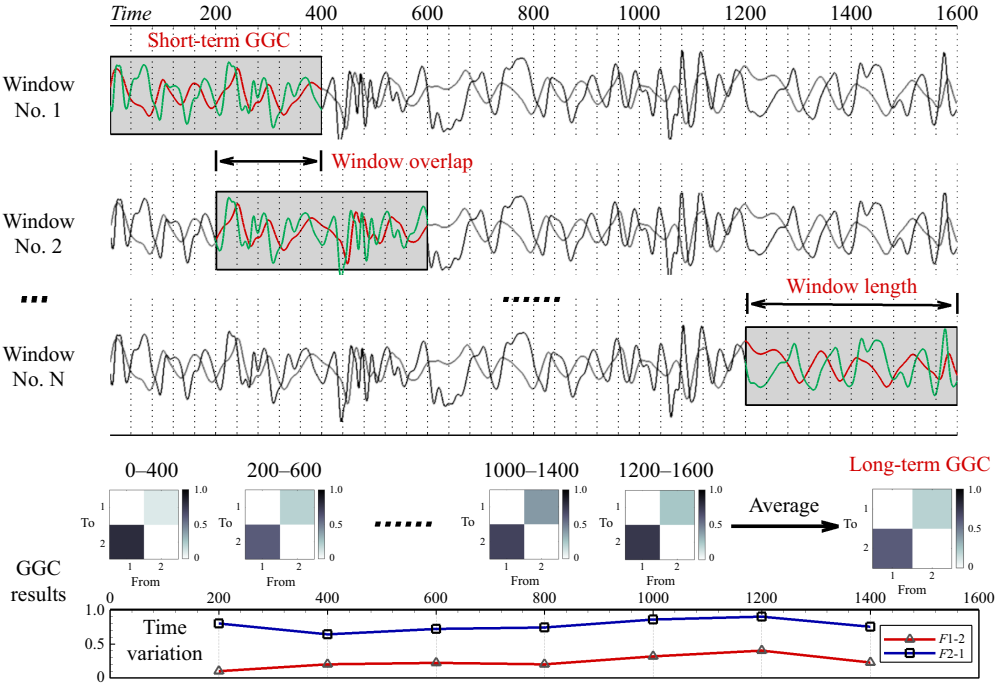


Figure 2. Schematic of the windowed analysis strategy of GGC. The time series of variables are equidistantly partitioned into intervals, with Granger causality applied to each interval to capture short-term causality, which are then ensemble-averaged to derive the averaged causality.

removing all linear and quadratic terms involving mode p, the reduced Galerkin model is constructed:

$$\boldsymbol{x}_q^t = \sum_{i=1}^{n} \tilde{L}_i \boldsymbol{x}_i^{t-1} + \sum_{i,j=1,i\leqslant j}^{n} \tilde{Q}_{ij} \boldsymbol{x}_i^{t-1} \boldsymbol{x}_j^{t-1} + \tilde{C} + \tilde{\boldsymbol{\varepsilon}}_{p\to q} \quad (i,\, j \neq p), \tag{4.2}$$

where the constraint $i,\, j \neq p$ excludes all terms involving mode p and $\tilde{\boldsymbol{\varepsilon}}_{p\to q}$ is the corresponding error vector. In accordance with the classical Granger causality, $\mathcal{F}_{p\to q}$ in each analysis window is defined as the log-ratio of two variances:

$$\mathcal{F}^i_{p\to q} = \ln \frac{\mathrm{var}(\tilde{\boldsymbol{\varepsilon}}_{p\to q})}{\mathrm{var}(\boldsymbol{\varepsilon}_q)}, \quad i = 1, 2, 3, \ldots, N, \tag{4.3}$$

where self-causalities $\mathcal{F}_{i\to i}$ are not computed and manually set to 0. By repeating the process in all windows, the short-term GGC for each window is obtained. Notably, this formulation allows for parallel computing, offering an advantage in computational speed. Taking the average of the results from all analysis windows, we obtain the long-term GGC of the entire sequence:

$$\mathcal{F}_{p\to q} = \mathrm{avg}(\mathcal{F}^1_{p\to q} + \mathcal{F}^2_{p\to q} + \cdots + \mathcal{F}^N_{p\to q}). \tag{4.4}$$

The CDI is then defined as

$$\mathrm{CDI} = \frac{\mathrm{std}(\mathcal{F}_{p\to q})}{\mathrm{avg}(\mathcal{F}_{p\to q})} = \sqrt{\frac{1}{m-1}\sum_{p,q=1}^{n} \left(\mathcal{F}_{p\to q} - \overline{\mathcal{F}}\right)^2 / \overline{\mathcal{F}}}, \quad p \neq q, \tag{4.5}$$

https://doi.org/10.1017/jfm.2026.11553 Published online by Cambridge University Press

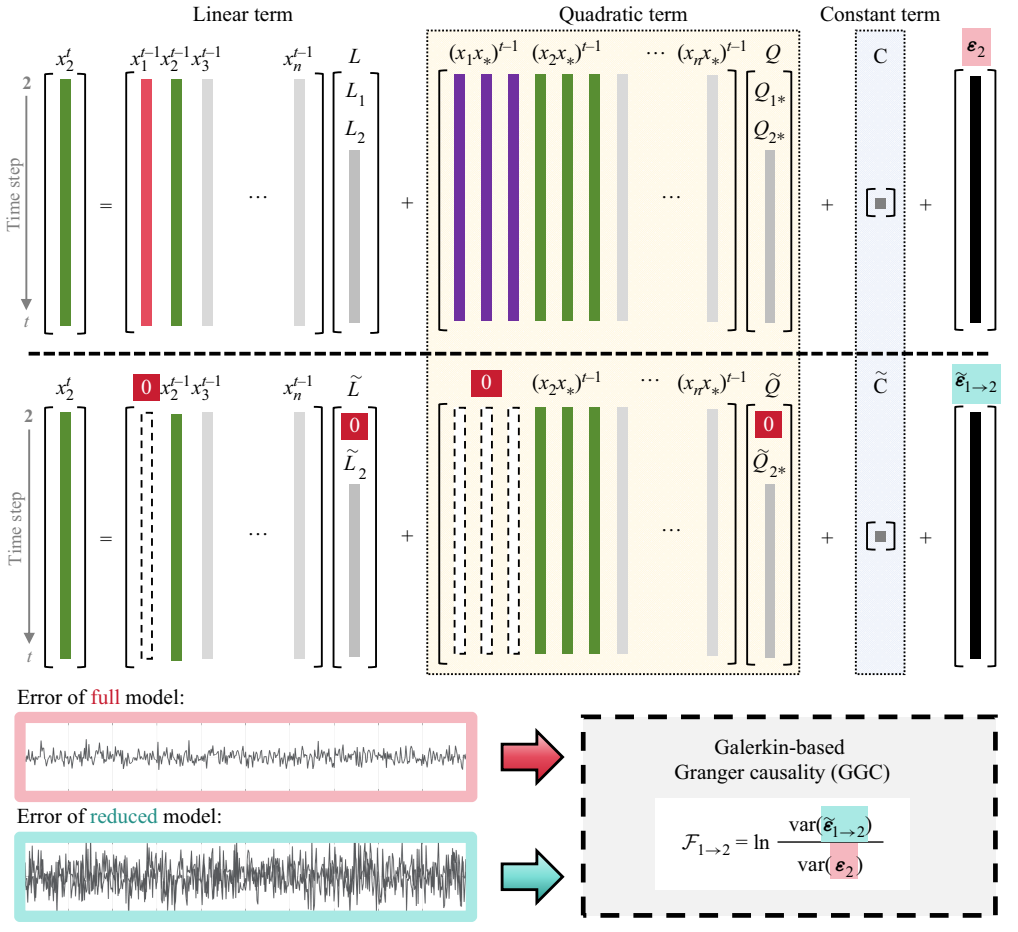


Figure 3. Schematic illustration of modified Granger causality. The framework retains the core structure of classical Granger causality, with the addition of nonlinear and constant terms to align with the structure of Galerkin equations.

where $m = n(n-1)$ represents the number of pairwise GGC, $\mathrm{avg}(\mathcal{F}_{i\to j}) = \overline{\mathcal{F}} = (1/m)\sum_{i,j=1}^{n}(\mathcal{F}_{i\to j})$, $i \neq j$ represents the overall mean GGC value and $\mathrm{std}(\mathcal{F}_{i\to j})$ denotes the overall standard deviation. Therefore, the CDI is defined as the ratio of the standard deviation to the mean GGC value, quantifying the discriminability of pairwise causality. An optimal window length enhances the distinction between strong and weak causal links, resulting in a higher CDI (see figure 10). Thus, we determine the window length by maximising the CDI.

Statistical tests are essential for distinguishing true causal relationships from spurious ones in causal inference. Standard tests for Granger causality, the F-test and likelihood ratio test (Shojaie & Fox 2022), can be extended to our proposed GGC framework. However, when applied to nonlinear flow data, both tend to overestimate the significance and produce false positives, as detailed in the supplementary material availabe at https://doi.org/10.1017/jfm.2026.11553. As an alternative, we employ a permutation test based on time-shifted surrogates (Quian Quiroga *et al.* 2002; Andrzejak *et al.* 2003), which effectively removes secondary and spurious causalities. Its core idea is simple: for each candidate cause variable, we generate multiple surrogate time series by applying

https://doi.org/10.1017/jfm.2026.11553 Published online by Cambridge University Press

random cyclic time shifts (i.e. rotating the time series by a random lag; see figure 11*c*). This procedure breaks any potential causality from the cause variable while preserving the intrinsic statistical properties of each series. We then compute GGC for plenty of these shifted surrogate pairs (typically 50–200 permutations) to construct an empirical null distribution under the hypothesis of no Granger causality. The $(1-\alpha)$th quantile (e.g. the 95th percentile for $\alpha = 0.05$) of this distribution is taken as the significance threshold. If the GGC value from the original data exceeds this threshold, we reject the null hypothesis and conclude that statistically significant Granger causality exists at level α. This allows us to reliably identify causal links from the quantitative GGC results.

We also emphasise some limitations of the proposed GGC method. (i) The quadratic formulation is specifically designed for Galerkin models of fluid flows and may not generalise to systems with different dynamical structures. (ii) Results can be influenced by hyperparameters such as window length and significance level in permutation tests, making careful selection and sensitivity analysis necessary before analysing the causal relations. (iii) In systems dominated by quadratic terms, GGC quantifies blended multivariate causal effect rather than isolated pairwise causality. For example, the quadratic term $a_j a_k$ of $\dot{a}_i$ inherently contains coupled influence from both a_j and a_k to a_i, which cannot be distinguished independently. However, this is due to the strong coupling between triadic mode pairs (Kraichnan & Chen 1989) in Galerkin models. Enforcing strict pairwise causality (e.g. by omitting interaction terms) would thus fail to capture the true dynamics.

5. Application

In this section, the proposed GGC is validated through the application to an empirical Galerkin model for turbulent shear flows proposed by Moehlis *et al.* (2004). We begin by analysing the governing equations (i.e. the first principles) to represent the reference causality (§ 5.2). Next, we apply GGC to the same model based on simulation data, and show that the inferred causality closely matches the reference (§ 5.3). Through these analyses, we validate GGC and the robustness of the combined analysis. Useful insights into the causal interactions among Galerkin modes are also obtained. Then, causality-guided flow control is investigated to show how the analysis helps to distill control opportunities (§ 5.4). Finally, a comparison between the GGC and existing causal analysis methods is provided (§ 5.5).

5.1. *Nine-equation turbulent shear flow model*

Waleffe (1997) developed an eight-Fourier-mode ROM for turbulent shear flows based on Galerkin projection. This empirical model was later refined by Moehlis *et al.* (2004), where the ninth mode is introduced for correction. This model depicts three-dimensional turbulent shear flow induced by sinusoidal body forcing. The velocity is composed of nine Fourier velocity modes: the base profile (mode 1), streak (mode 2), downstream vortex (mode 3), spanwise flow (modes 4 and 5), normal vortex (modes 6 and 7), fully three-dimensional structure (mode 8) and modification of the base profile (mode 9), as shown in figure 4. Their detailed descriptions are presented in Appendix B. The spatial domain is specified as $0 \leqslant x \leqslant L_x$, $-1 \leqslant y \leqslant 1$, $0 \leqslant z \leqslant L_z$. By projecting the incompressible Navier–Stokes equations onto the nine velocity modes, the following system of ODEs is derived:

$$\frac{\mathrm{d}a_1}{\mathrm{d}t} = \frac{\beta^2}{Re} - \frac{\beta^2}{Re}a_1 - \sqrt{\frac{3}{2}}\frac{\beta\gamma}{\kappa_{\alpha\beta\gamma}}a_6 a_8 + \sqrt{\frac{3}{2}}\frac{\beta\gamma}{\kappa_{\beta\gamma}}a_2 a_3, \tag{5.1}$$

https://doi.org/10.1017/jfm.2026.11553 Published online by Cambridge University Press

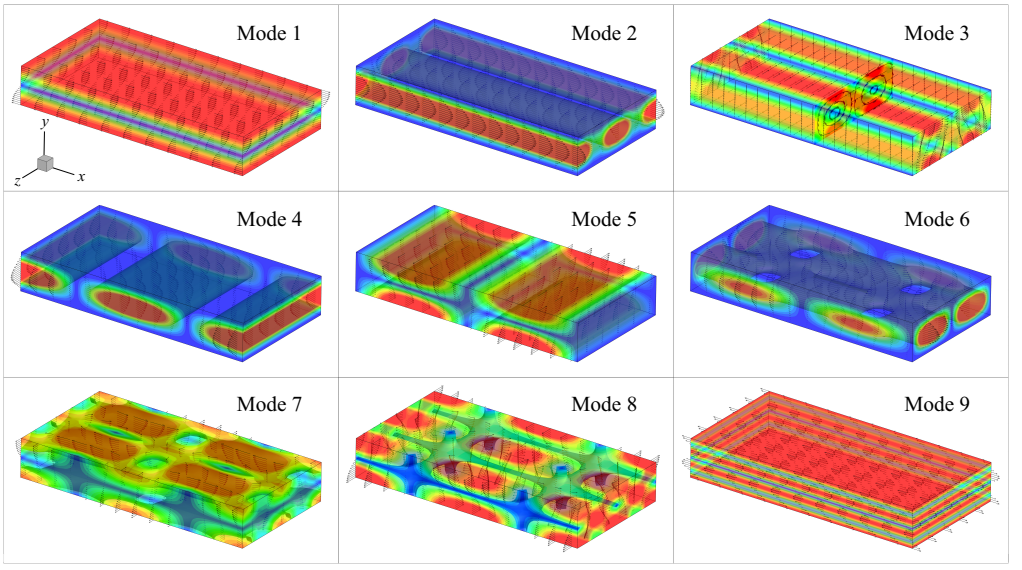


Figure 4. Velocity contours of the nine modes in the turbulent shear flow model. Arrows denote velocity vectors, while the colour map (blue: low; red: high) indicates velocity magnitude.

$$\frac{\mathrm{d}a_2}{\mathrm{d}t} = -\left(\frac{4\beta^2}{3}+\gamma^2\right)\frac{a_2}{Re} + \frac{5\sqrt{2}}{3\sqrt{3}}\frac{\gamma^2}{\kappa_{\alpha\gamma}}a_4a_6 - \frac{\gamma^2}{\sqrt{6}\kappa_{\alpha\gamma}}a_5a_7 - \frac{\alpha\beta\gamma}{\sqrt{6}\kappa_{\alpha\gamma}\kappa_{\alpha\beta\gamma}}a_5a_8 - \sqrt{\frac{3}{2}}\frac{\beta\gamma}{\kappa_{\beta\gamma}}a_1a_3 - \sqrt{\frac{3}{2}}\frac{\beta\gamma}{\kappa_{\beta\gamma}}a_3a_9, \tag{5.2}$$

$$\frac{\mathrm{d}a_3}{\mathrm{d}t} = -\frac{\beta^2+\gamma^2}{Re}a_3 + \frac{2}{\sqrt{6}}\frac{\alpha\beta\gamma}{\kappa_{\alpha\gamma}\kappa_{\beta\gamma}}(a_4a_7+a_5a_6) + \frac{\beta^2(3\alpha^2+\gamma^2)-3\gamma^2(\alpha^2+\gamma^2)}{\sqrt{6}\kappa_{\alpha\gamma}\kappa_{\beta\gamma}\kappa_{\alpha\beta\gamma}}a_4a_8, \tag{5.3}$$

$$\frac{\mathrm{d}a_4}{\mathrm{d}t} = -\frac{3\alpha^2+4\beta^2}{3Re}a_4 - \frac{10}{3\sqrt{6}}\frac{\alpha^2}{\kappa_{\alpha\gamma}}a_2a_6 - \sqrt{\frac{3}{2}}\frac{\alpha\beta\gamma}{\kappa_{\alpha\gamma}\kappa_{\beta\gamma}}a_3a_7 - \sqrt{\frac{3}{2}}\frac{\alpha^2\beta^2}{\kappa_{\alpha\gamma}\kappa_{\beta\gamma}\kappa_{\alpha\beta\gamma}}a_3a_8 - \frac{\alpha}{\sqrt{6}}a_1a_5 - \frac{\alpha}{\sqrt{6}}a_5a_9. \tag{5.4}$$

$$\frac{\mathrm{d}a_5}{\mathrm{d}t} = -\frac{\alpha^2+\beta^2}{Re}a_5 + \frac{\alpha}{\sqrt{6}}a_1a_4 + \frac{\alpha^2}{\sqrt{6}\kappa_{\alpha\gamma}}a_2a_7 - \frac{\alpha\beta\gamma}{\sqrt{6}\kappa_{\alpha\gamma}\kappa_{\alpha\beta\gamma}}a_2a_8 + \frac{\alpha}{\sqrt{6}}a_4a_9 + \frac{2}{\sqrt{6}}\frac{\alpha\beta\gamma}{\kappa_{\alpha\gamma}\kappa_{\beta\gamma}}a_3a_6, \tag{5.5}$$

$$\frac{\mathrm{d}a_6}{\mathrm{d}t} = -\frac{3\alpha^2+4\beta^2+3\gamma^2}{3Re}a_6 + \frac{\alpha}{\sqrt{6}}a_1a_7 + \sqrt{\frac{3}{2}}\frac{\beta\gamma}{\kappa_{\alpha\beta\gamma}}a_1a_8 + \frac{10}{3\sqrt{6}}\frac{\alpha^2-\gamma^2}{\kappa_{\alpha\gamma}}a_2a_4 - 2\sqrt{\frac{2}{3}}\frac{\alpha\beta\gamma}{\kappa_{\alpha\gamma}\kappa_{\beta\gamma}}a_3a_5 + \frac{\alpha}{\sqrt{6}}a_7a_9 + \sqrt{\frac{3}{2}}\frac{\beta\gamma}{\kappa_{\alpha\beta\gamma}}a_8a_9, \tag{5.6}$$

https://doi.org/10.1017/jfm.2026.11553 Published online by Cambridge University Press

Parameter	Explanation	Value
L_x	Length of the domain in the x direction	4π
L_z	Length of the domain in the z direction	2π
Re	Reynolds number	400
dt	Time step	0.1
Time	Total time of evolution	1.2×10^4

Table 1. Parameter settings for the turbulent shear flow model.

$$\frac{\mathrm{d}a_7}{\mathrm{d}t} = -\frac{\alpha^2+\beta^2+\gamma^2}{Re}a_7 - \frac{\alpha}{\sqrt{6}}(a_1a_6 + a_6a_9) + \frac{1}{\sqrt{6}}\frac{\gamma^2-\alpha^2}{\kappa_{\alpha\gamma}}a_2a_5 + \frac{1}{\sqrt{6}}\frac{\alpha\beta\gamma}{\kappa_{\alpha\gamma}\kappa_{\beta\gamma}}a_3a_4, \tag{5.7}$$

$$\frac{\mathrm{d}a_8}{\mathrm{d}t} = -\frac{\alpha^2+\beta^2+\gamma^2}{Re}a_8 + \frac{2}{\sqrt{6}}\frac{\alpha\beta\gamma}{\kappa_{\alpha\gamma}\kappa_{\alpha\beta\gamma}}a_2a_5 + \frac{\gamma^2(3\alpha^2-\beta^2+3\gamma^2)}{\sqrt{6}\kappa_{\alpha\gamma}\kappa_{\beta\gamma}\kappa_{\alpha\beta\gamma}}a_3a_4, \tag{5.8}$$

$$\frac{\mathrm{d}a_9}{\mathrm{d}t} = -\frac{9\beta^2}{Re}a_9 + \sqrt{\frac{3}{2}}\frac{\beta\gamma}{\kappa_{\beta\gamma}}a_2a_3 - \sqrt{\frac{3}{2}}\frac{\beta\gamma}{\kappa_{\alpha\beta\gamma}}a_6a_8, \tag{5.9}$$

where Re denotes the Reynolds number, and constants are defined as

$$\begin{gathered}\alpha = 2\pi/L_x, \quad \beta = \pi/2, \quad \gamma = 2\pi/L_z, \\ \kappa_{\alpha\gamma} = \sqrt{\alpha^2+\gamma^2}, \quad \kappa_{\beta\gamma} = \sqrt{\beta^2+\gamma^2}, \quad \kappa_{\alpha\beta\gamma} = \sqrt{\alpha^2+\beta^2+\gamma^2}.\end{gathered} \tag{5.10}$$

The system of ODEs is numerically integrated using a fourth-order Runge–Kutta scheme with parameters specified in table 1. The temporal evolution of mode coefficients starting from initial condition [0, 0.1, 0.1, 0.1, 0.1, 0, 0, 0, 0] is shown in figure 5, which exhibits chaotic characteristics, eventually converging to a steady-state equilibrium. Throughout the transition phase, intermittent bursts of intense variations are observed. These transient bursts are defined as extreme events (Sapsis 2021), as shown in figure 6. Due to its simplicity and various turbulence characteristics, including multiscale fluctuations, energy dissipation and relaminarisation, this model has become a benchmark for studying transition (Skufca, Yorke & Eckhardt 2006), turbulence modelling (Srinivasan *et al.* 2019) and flow control (Racca & Magri 2022).

5.2. *Equation-based causal analysis*

From the mathematical and physical principles of the Galerkin projection (see § 2), we can identify the causal relationships among modes. Inspecting the nonlinear terms in (5.1)–(5.9), the following two types of quadratic modal interactions are identified, and their associated causal relationships can lead to a directed cause-and-effect network of nonlinear dynamics.

(i) Modulated two-mode coupling: the mutual interaction of two modes controlled by a third mode whose evolution remains independent of the other two, as illustrated in figure 7(*a*). For instance, consider the nonlinear interactions among modes 1, 2 and 3.

https://doi.org/10.1017/jfm.2026.11553 Published online by Cambridge University Press

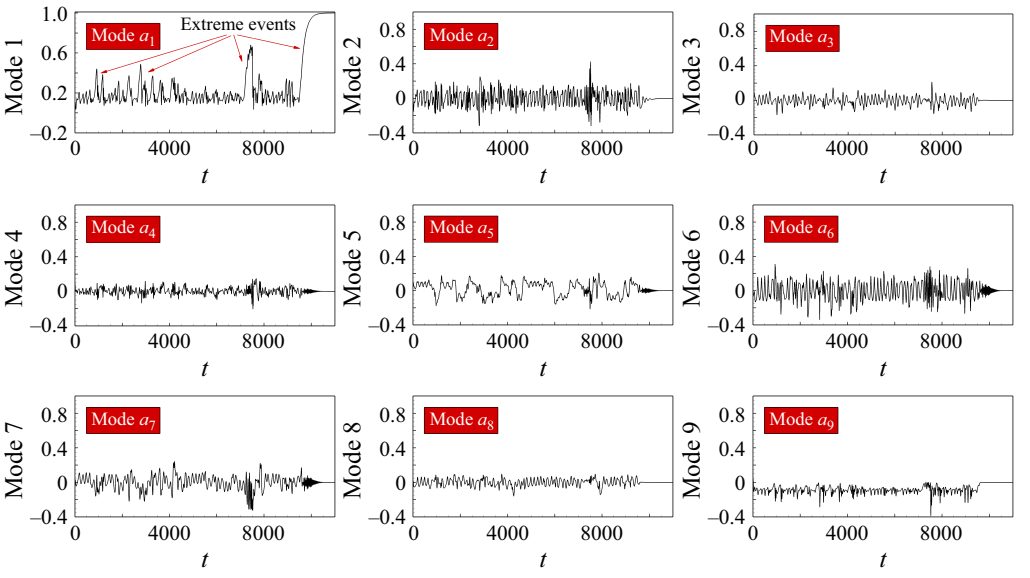


Figure 5. Temporal evolution of mode coefficients. Several extreme events burst throughout turbulence evolution. The system ultimately relaxes to a steady-shear-flow state after 10^4 time units.

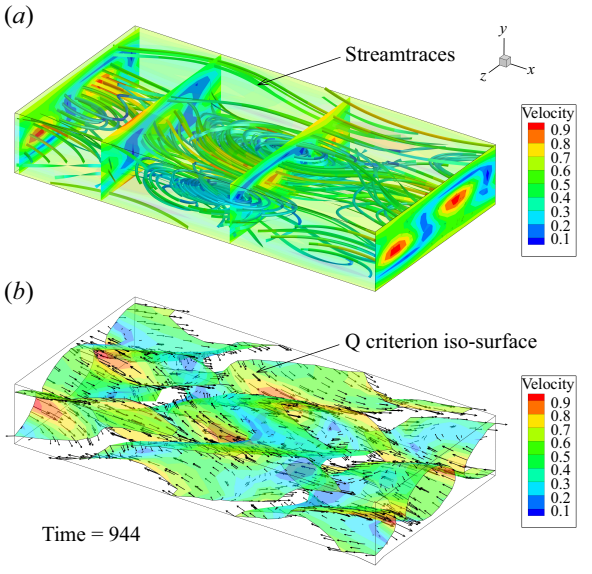


Figure 6. Instantaneous flow visualisation at $t = 944$. (*a*) Streamline and clipping plane contour. (*b*) Vortex topology revealed by Q-criterion iso-surfaces.

It can be observed that the governing equations of modes 1 and 2 mutually contain quadratic terms with coefficients of opposite signs (i.e. $Q_{123} = -Q_{213}$), while mode 3 lacks terms involving mode 1 or 2 (i.e. $Q_{321} = 0$). The energy conservation is thus maintained by $Q_{123} + Q_{213} + Q_{321} = 0$. Therefore, modes 1 and 2 form a transfer pair, with mode 3 acting as a catalyst that facilitates their interaction and energy transfer, defined as the modulator. This phenomenon physically represents a self-sustaining process (Waleffe 1997) in turbulent shear flow, where streamwise rolls

https://doi.org/10.1017/jfm.2026.11553 Published online by Cambridge University Press

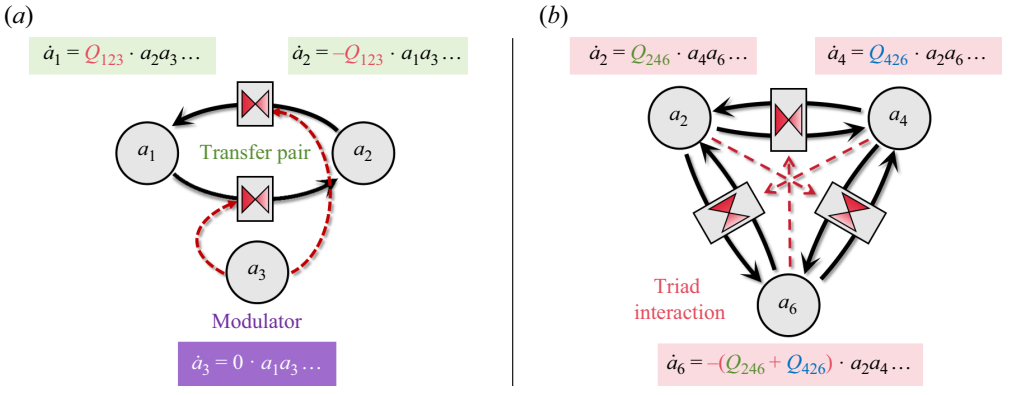


Figure 7. Schematic of two types of modal interaction. (*a*) Modulated two-mode coupling. (*b*) Triad interaction.

redistribute the mean shear flow to create streaks. Such a relationship is shown in figure 8, denoted as $[a_1 \rightleftharpoons a_2]a_3$, with analogous instances including $[a_1 \rightleftharpoons a_6]a_8$, $[a_4 \rightleftharpoons a_5]a_1$, etc. From the perspective of causality, this interaction consists of four causal relations: a bidirectional causality within the transfer pair and two unidirectional causalities from the modulator to the two pair modes separately.

(ii) Triad interaction: the mutual coupling among three modes, where each mode acts as a modulator for the interaction of the other two modes, as illustrated in figure 7(*b*). In the present model, modes 2, 4 and 6 form a triad interaction, appearing in each other's governing equations with quadratic term coefficients that strictly sum to zero ($Q_{246} + Q_{426} + Q_{624} = 0$). This principle governs mutual energy transfer between modes while conserving the total energy (Kraichnan & Chen 1989; Noack *et al.* 2008; Loiseau & Brunton 2018). This relationship is denoted as $\mathcal{T}(a_2, a_4, a_6)$ with analogous instances including $\mathcal{T}(a_3, a_5, a_6)$, $\mathcal{T}(a_3, a_4, a_7)$ etc. Within the triad interaction, each pair of modes exhibits mutual causation, resulting in three bidirectional causalities. Notably, here the causality is defined as the direct cause-and-effect between modes. The absence of such causality does not preclude the possibility of indirect interactions, which may occur through intermediate modes.

All quadratic interactions identified in the turbulent shear flow model are summarised in table 2, which also leads to a directed causal network shown in figure 9(*a*) and a causal map shown in figure 9(*b*). Equation-based causal analysis grounded in rigorous mathematical and physical foundations of the Galerkin model provides reliable insights into causal relationships. However, this approach only provides qualitative results but fails to quantify the magnitude of them. Furthermore, the turbulent shear flow model examined in this study remains simple, i.e. a Fourier-based Galerkin model with sparse and well-structured equations. For complex real-world flows, such an ideal Galerkin model is very difficult to construct, which obscures the application of equation-based analysis in practice. However, empirical Galerkin models using truncated POD bases can also be obtained as the reference model for equation-based analysis, given that the sparse model structure is correctly extracted (Loiseau & Brunton 2018).

5.3. *Galerkin-based Granger causality analysis*

This section focuses on the identification of causal relationships from data, using the proposed GGC approach. To enhance flow stability, we analyse data generated at a higher

https://doi.org/10.1017/jfm.2026.11553 Published online by Cambridge University Press

Fundamental modal interactions	Instance
Modulated two-mode coupling	$[a_1 \rightleftharpoons a_2]a_3$, $[a_2 \rightleftharpoons a_9]a_3$, $[a_1 \rightleftharpoons a_6]a_8$, $[a_6 \rightleftharpoons a_9]a_8$, $[a_4 \rightleftharpoons a_5]a_1$, $[a_4 \rightleftharpoons a_5]a_9$, $[a_6 \rightleftharpoons a_7]a_1$, $[a_6 \rightleftharpoons a_7]a_9$
Triad interaction	$\mathcal{T}(a_2, a_4, a_6)$, $\mathcal{T}(a_2, a_5, a_7)$, $\mathcal{T}(a_2, a_5, a_8)$, $\mathcal{T}(a_3, a_5, a_6)$, $\mathcal{T}(a_3, a_4, a_7)$, $\mathcal{T}(a_3, a_4, a_8)$

Table 2. Summary of identified modal interactions in turbulent shear flow model.

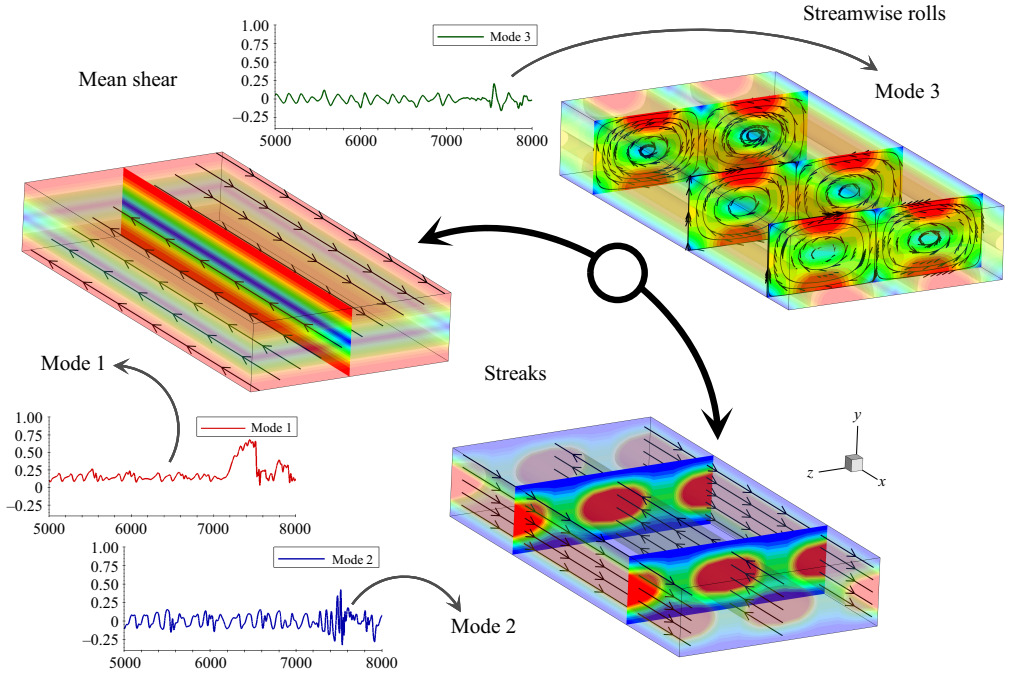


Figure 8. Interaction between the main shear flow (mode 1) and streaks (mode 2), modulated by the streamwise rolls (mode 3). Three-dimensional mode contours and the temporal evolution of mode coefficients are depicted, illustrating the dynamic interaction between modes.

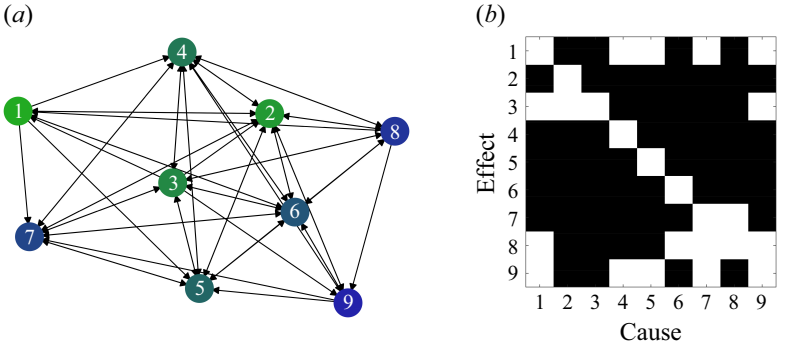


Figure 9. Equation-based causal network of the turbulent shear flow model. (*a*) Overall causal links across all modes. Arrow convention: one-way arrows indicate unidirectional causal influence; two-way arrows denote bidirectional causal interactions. (*b*) Visualised in a 9×9 causal map.

https://doi.org/10.1017/jfm.2026.11553 Published online by Cambridge University Press

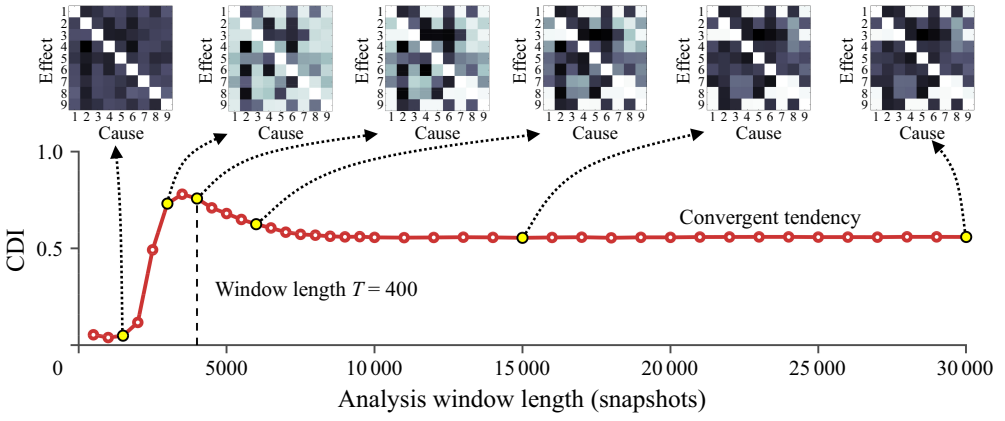


Figure 10. Determination of the window length, representing the trade-off between time-variant resolution and causal discriminability, where a length of 4000 snapshots (400 time units) yields the optimal outcome.

Reynolds number $Re = 600$, starting from the initial condition [0, 0.1,0.1, 0.1,0.1, 0, 0, 0, 0]. The hyperparameter, i.e. the optimal sampling window, should be determined first. The relationship between CDI and window length is investigated, as illustrated in figure 10. The CDI gradually increases until peaking at around $T = 400$, then it gradually declines to a steady value at around $T = 1000$. Therefore, the window length is set to 400, corresponding to the maximum CDI value and a clearest causal pattern. It ensures sufficient model accuracy while maximising the cause-and-effect identification among strong causality, weak causality and non-causality.

As shown in figure 11(a), the GGC results provide a quantitative measure of Granger causality. However, to determine which causal interactions actually exist, a binary (0–1) causal map is required. This can be derived from the GGC results using either threshold-based classification or permutation test. In the threshold-based classification, a cutoff value is selected, and causal links with GGC values above this threshold are labelled as 'true', while others are labelled 'false'. A common heuristic is to rank all GGC values and choose the threshold at the 'elbow', i.e. the point where the decay curve begins to flatten. For the current problem, this yields a threshold of 0.15, as shown in figure 11(b). Practically, this approach is empirical and relies on expert knowledge. A more rigorous alternative is to apply a permutation test (introduced in § 4). As shown in figure 12, using 100 permutations and a significance level of $\alpha = 0.1$, the resulting binary causal map exactly matches the ground-truth causality derived from the governing equations (figure 9). These findings validate the reliability of GGC. Furthermore, using the proposed GGC, one can also identify mode interactions purely from data, if the Galerkin-based model is not available or too complex.

Based on its definition, the GGC value quantifies the informative contribution of a given mode to the dynamic prediction of other modes. We then take the column-wise sum of outgoing GGC values from each mode as its 'causal importance'. Physically, it reflects the mode's overall informative contribution in the system. Notably, its relative ranking and pattern are more meaningful than absolute magnitudes. As shown in figure 14, modes 2 and 6 exhibit the highest score, underscoring their critical roles in the system. This can also be supported by the fact that energy is input through mode 1 (the base profile), and modes 2 (streak) and 6 (normal vortex) play a crucial role in transferring energy from mode 1 to the rest of the system. With this quantification, users can rapidly detect modes that

https://doi.org/10.1017/jfm.2026.11553 Published online by Cambridge University Press

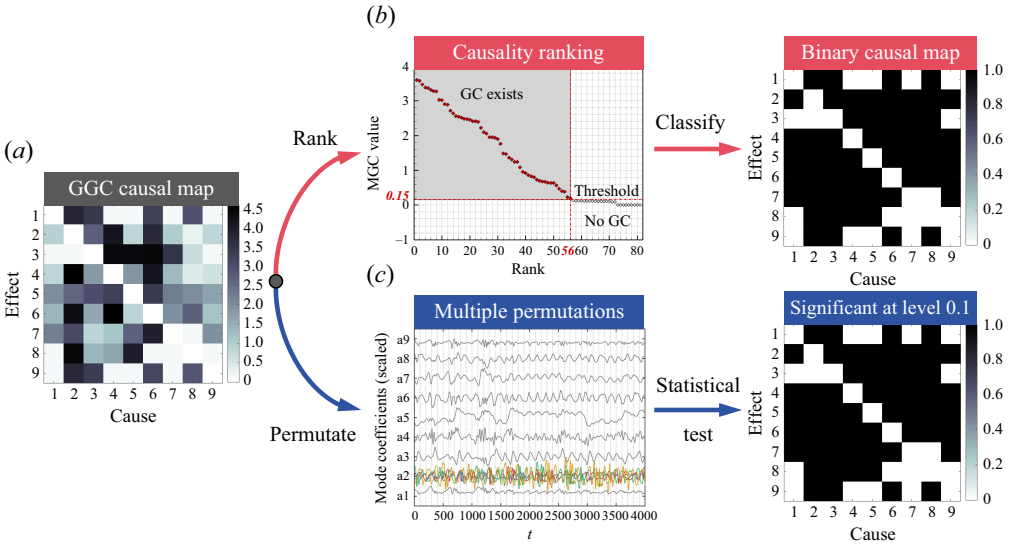


Figure 11. (*a*) The GGC result of shear flow model; (*b*) causality ranking and the identification of a threshold value (0.15 in this case), where the decay of GGC shows a tendency of stagnation; (*c*) binary causal map extracted from permutation test, which is detailed in § 4. The resulting binary causal map shows absolute agreement with equation-based analysis, validating the reliability of GGC.

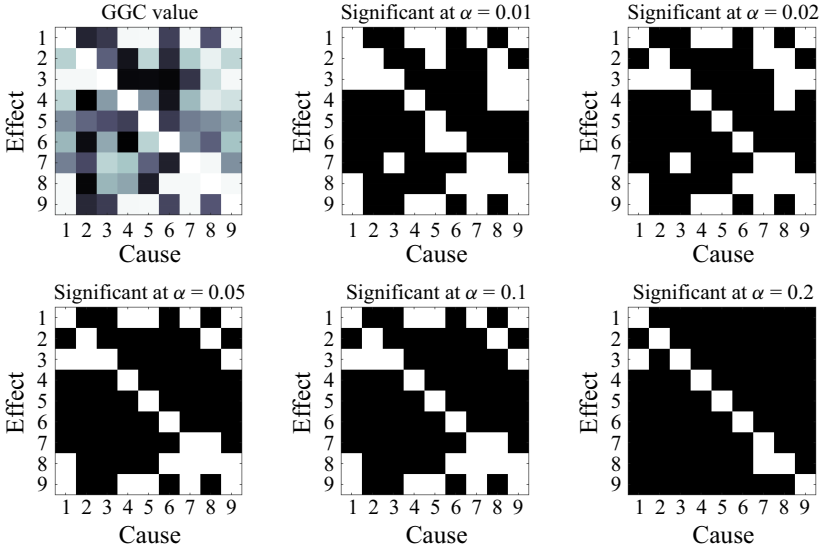


Figure 12. Permutation tests at different significance levels on the shear flow model (100 permutations). Satisfactory causal identification is achieved for conventional levels 0.05 and 0.1, while misclassifications arise at extreme significance levels.

are causally important. The ROMs built from these key modes can capture the essential behaviour of the system, which needs to be modelled with a high level of accuracy.

By varying the initial conditions, Reynolds number and window length, we obtained four sets of data samples. These samples are analysed using GGC, classical Granger causality (implemented with the MVGC toolbox (Barnett & Seth 2014) without

https://doi.org/10.1017/jfm.2026.11553 Published online by Cambridge University Press

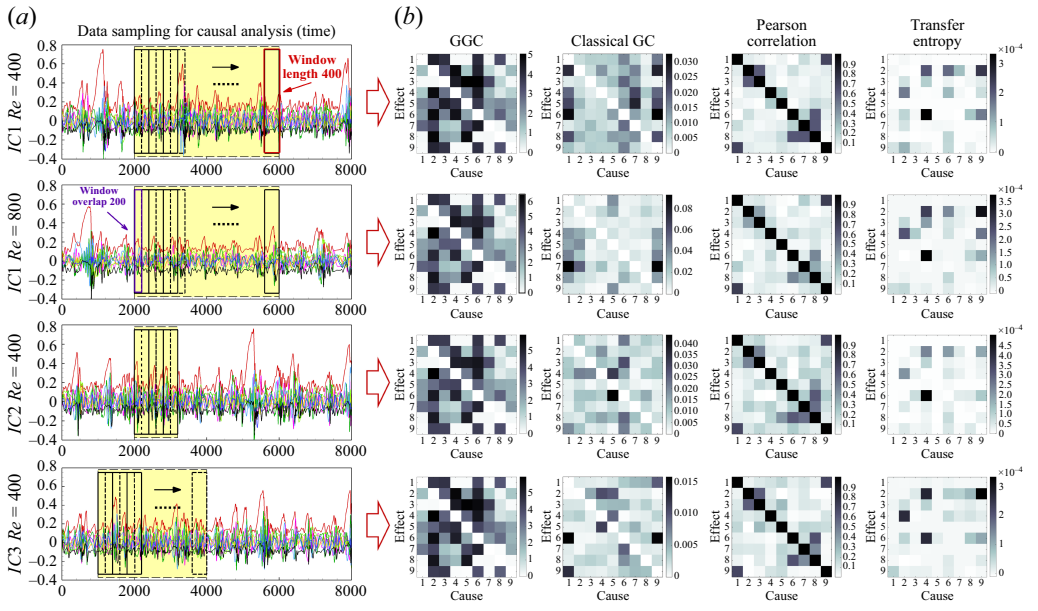


Figure 13. Comparison of GGC, classical Granger causality, Pearson correlation and transfer entropy. (*a*) Four distinct modal evolution sequences, each corresponding to a unique set of initial conditions and Reynolds numbers. The yellow boxes indicate the windowed sampling used for GGC analysis. (*b*) The results from the four methods are displayed sequentially (self-causality terms are omitted by definition for causal analysis (GGC/Granger causality/transfer entropy)). The GGC is shown to be the most accurate and robust across all cases.

analysis windows), Pearson correlation and transfer entropy (implemented via codes of Martínez-Sánchez *et al.* (2023)) to examine causal relationships between modes. The results are shown in figure 13. We observe significant variations in the results of classical Granger causality across the four datasets, indicating its robustness deficiency. This further demonstrates that the classical Granger causality, as a linear method, is unreliable for discovering causality in nonlinear systems. In contrast, the GGC produced highly consistent results across all datasets, demonstrating strong robustness. This confirms that our modifications to the Granger causality method are both reasonable and effective. Pearson correlation and transfer entropy also yield robust results, but the former reflects only trend similarity (not causality), and the latter recovers fewer causal links than the ground-truth dynamics.

Finally, GGC is also applicable to complex, high-dimensional flows where a Galerkin-projected model is hard to obtain. As a demonstration, we apply it to analyse the causal structure of a turbulent lid-driven cavity flow (Arbabi & Mezić 2017), which is detailed in Appendix B.

5.4. *Causality-guided flow control*

This section demonstrates how causal findings in §§ 5.2 and 5.3 offer valuable insights for flow control. At low Reynolds numbers, extreme events (formulated as strong relaminarisation) emerge in the present turbulent shear flow model. Racca & Magri (2022) employed echo state networks to predict the evolution of mode coefficients and successfully suppressed extreme events before their onset. Inspired by this work, we

https://doi.org/10.1017/jfm.2026.11553 Published online by Cambridge University Press

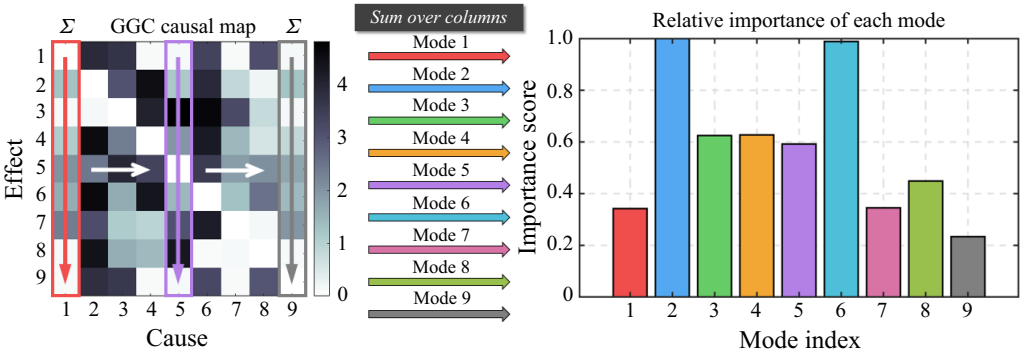


Figure 14. The column sum of the GGC causal map is defined as the causal importance of each mode, representing the total Granger causality exerted by that mode on all other modes.

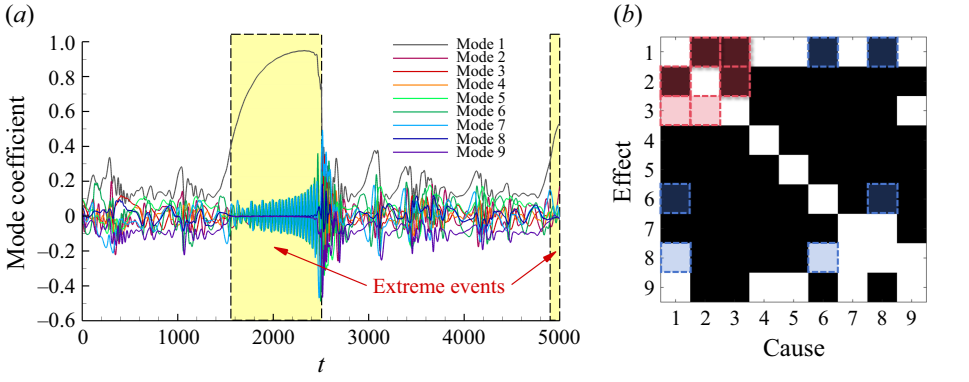


Figure 15. (*a*) Time evolution of the shear flow mode coefficients, illustrating extreme events as sharp increases in the amplitude of mode 1 (highlighted in yellow). The corresponding flow contours during these events are shown in figure 17(*b–d*). (*b*) Binary causal map. Red and blue boxes highlight the modulated two-mode coupling involving modes 1, 2, 3 and modes 1, 6, 8, respectively. In both cases, modes 3 and 8 act as modulators.

approach the same problem from a causal perspective. Specifically, we show that applying control body forces to mode 3 or mode 8 (modulating modes) enables robust suppression of extreme events. The following flow control is conducted at $Re = 600$, starting from a random initial condition of [0, 0.03, 0.1, 0.05, 0.1, 0, 0, 0.04, 0].

As shown in figure 15(*a*), extreme events are characterised by a sharp increase in the amplitude of mode 1. To suppress such events, it is therefore necessary to extract energy from this mode. As previously introduced in § 5.2, mode 3 acts as a modulator for the energy transfer between modes 1 and 2 ($[a_1 \rightleftharpoons a_2]a_3$), and similarly, mode 8 modulates the transfer between modes 1 and 6 ($[a_1 \rightleftharpoons a_6]a_8$). These modulating modes (3 and 8) present themselves as the most effective leverage points for extracting energy from mode 1 to mitigate extreme events. Such a conclusion can also be drawn from the data-driven causal map shown in figure 15(*b*), as modes 2, 3, 6 and 8 are the only ones that cause mode 1. Specifically, modes 2 and 6 engage in a bidirectional interaction with mode 1, whereas modes 3 and 8 exert a unidirectional causal influence on it. This structural pattern suggests that modes 3 and 8 are possible modulators controlling the energy transfer between mode 1 and others.

https://doi.org/10.1017/jfm.2026.11553 Published online by Cambridge University Press

Algorithm 1. Suppression of extreme events in shear flow model

Parameters:
• Threshold : $a_{TH} \in (0.25, 1)$, threshold for control operation
• Control amplitude : $K \in (0.01, 1)$, magnitude of control body force
• Time step of control: $\mathrm{d}t_c \in (0.01, 0.1)$, time step for observation and control
Plant:
• Galerkin model for turbulent shear flow (Moehlis *et al.* 2004)
Control input:
• Apply control body force to mode 3 to suppress extreme events (if $a_1 > a_{TH}$)
Control objective:
• Maintain extreme events suppressed ($a_1 < a_{TH}$)

while true **do**
  if $a_1 > a_{TH}$ **then**
    $f_c = -K \cdot \mathrm{sgn}(a_2)$ // Bang-bang control
  else
    $f_c = 0$
  end if
  $\mathrm{d}a_3/\mathrm{d}t = \mathcal{L}(a_1, a_2, \ldots a_9) + f_c$ // Update mode 3 dynamics with control input
  Turbulence evolves one time step of control $\mathrm{d}t_c$
end while

Based on the insights extracted from causal analysis, we can develop a causality-guided flow control strategy: upon detection of an extreme event ($a_1 > a_{TH}$), a control body force is applied to the modulator (mode 3) to facilitate energy transfer from mode 1 to mode 2, thereby suppressing the extreme event. Specifically, to extract energy out of mode 1, the applied body force f_c is designed to oppose the instantaneous phase of mode 2. This yields the following expression:

$$f_c = \begin{cases} -K \cdot \mathrm{sgn}(a_2), & a_1 > a_{TH} \\ 0, & a_1 \leqslant a_{TH}, \end{cases} \tag{5.11}$$

where K represents the control amplitude and $\mathrm{sgn}(\cdot)$ denotes the sign function. Since the control amplitude is fixed, it is a typical bang-bang control (Bryson 2018). The complete flow control strategy is presented in Algorithm 1, which is defined by three parameters: threshold a_{TH}, control amplitude K and time step of control $\mathrm{d}t_c$. We also provide recommended ranges for the three parameters in Algorithm 1.

With $\mathrm{d}t_c = 0.1$ and $K = 0.1$, the proposed control algorithm effectively suppresses extreme events under various initial conditions and thresholds, as illustrated in figure 16(*a–c*). Further testing reveals that modifying the time step and control amplitude influences the response speed of the control system, thereby affecting the future evolution of the flow, as shown in figure 16(*d*,*e*). Despite these variations, the system remains capable of suppressing extreme events, demonstrating strong robustness. The operating time of the control system is notably brief, minimising both control costs and flow interference. The flow fields before and after suppressing extreme events are depicted in figure 17. It is shown that activation of the control system effectively maintains turbulent structures and suppresses extreme events.

Having demonstrated the effectiveness of controlling mode 3 to suppress the extreme events, we further apply the same strategy to another modulator (i.e. mode 8). By adding control body force on mode 8, energy is transferred from mode 1 to mode 6. Extreme events are again effectively suppressed, as shown in figure 18(*a*), indicating the robustness

https://doi.org/10.1017/jfm.2026.11553 Published online by Cambridge University Press

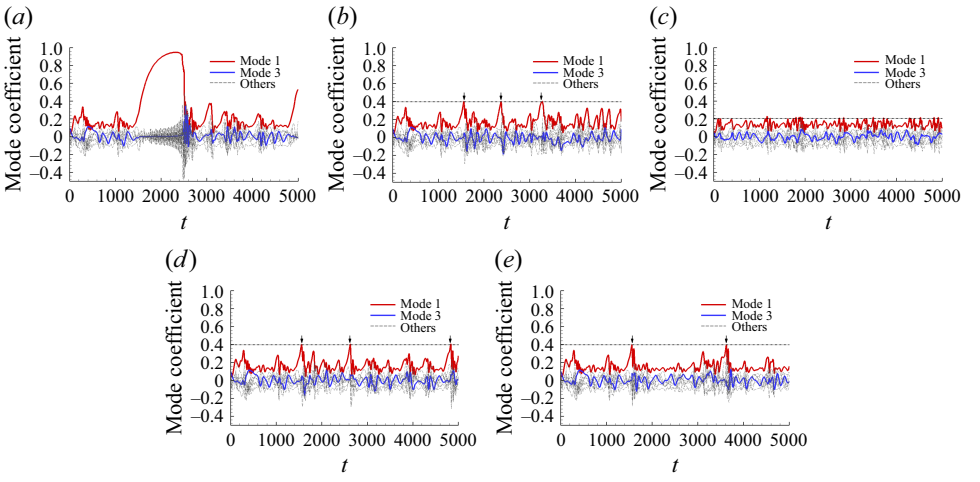


Figure 16. Suppression of extreme events by applying control body force to mode 3 under various conditions. The time step is set to $dt_c = 0.1$ in (*a–c*), with a control amplitude of $K = 0.01$. (*a*) The case without control, and the results of control thresholds set at (*b*) $a_{TH} = 0.4$ and (*c*) $a_{TH} = 0.2$. In (*d*), dt_c is reduced to 0.01. The control amplitude for (*e*) is increased to $K = 0.1$. Black arrows indicate positions where control is activated.

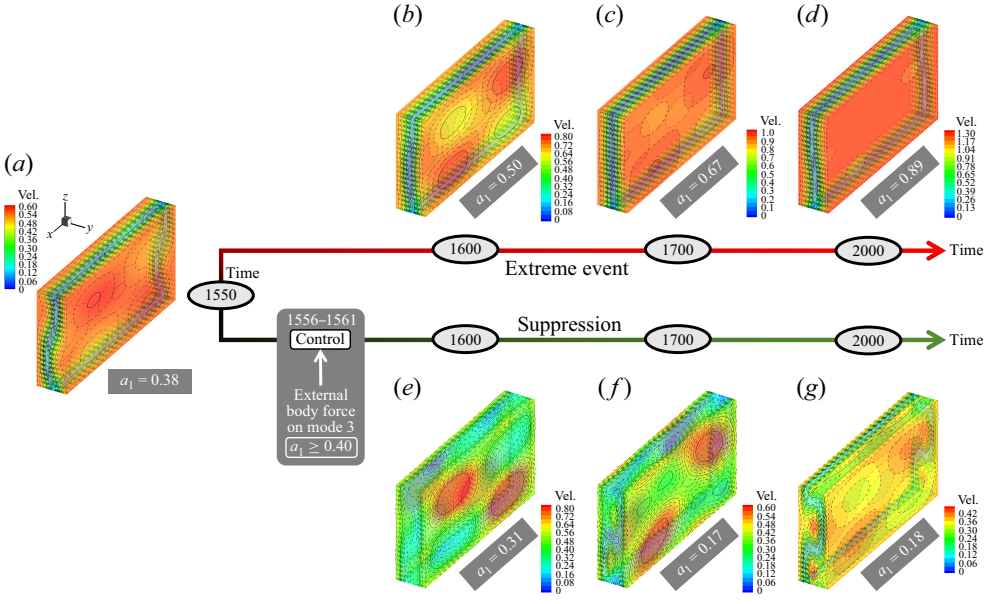


Figure 17. Snapshots of the flow field during an extreme event (corresponding to figure 16*a*,*b*), comparing uncontrolled (*b–d*) and controlled (*e–g*) scenarios. In the uncontrolled case, the flow exhibits a gradual decay towards a laminar shear flow. In contrast, the applied control rapidly suppresses this decay, maintaining turbulent structures and preventing laminarisation.

of the proposed causality-guided control. Although both modes 2 and 6 also cause mode 1, control attempts via these modes fail to suppress extreme events, as shown in figure 18(*b*,*c*). This failure is attributed to the fact that modes 2 and 6 form the transfer pair with mode 1; therefore they are not directly driving but rather participating in the energy transfer, making them ineffective as control actuators. Even without prior knowledge of

https://doi.org/10.1017/jfm.2026.11553 Published online by Cambridge University Press

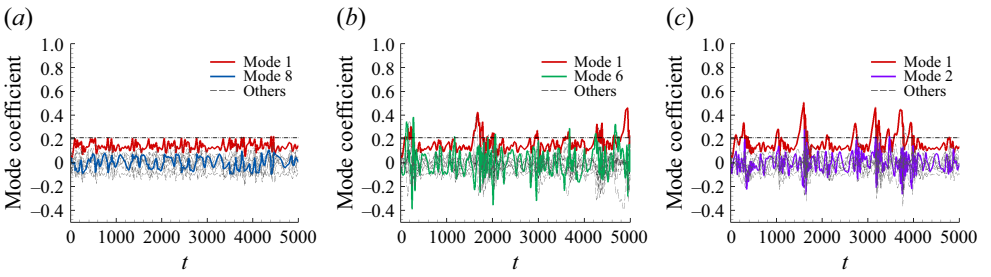


Figure 18. Suppression of extreme events under the same conditions as in figure 16(*c*), achieved by applying artificial body forces to (*a*) mode 8, (*b*) mode 6 and (*c*) mode 2. Successful suppression is observed only when control is applied to mode 8, which is also a modulating mode.

the system dynamics, these causal interactions can still be drawn directly from the causal map (figure 15*b*). This binary causal map clearly shows that modes 3 and 8 unidirectionally cause mode 1, whereas modes 2 and 6 engage in mutual interaction with it, rendering them less effective in control. These results highlight a key advantage of causal analysis: it not only reveals dynamical mechanisms but also provides valuable insights for control design.

5.5. *Comparisons with other methods*

Since standard Granger causality was proposed, numerous nonlinear extensions have been proposed and extensively studied, via incorporating kernels (Marinazzo, Pellicoro & Stramaglia 2008), radial basis functions (Ancona, Marinazzo & Stramaglia 2004), quadratic terms (Lopez-Doriga *et al.* 2024) or even neural networks (Tank *et al.* 2021). While these methods enhance the flexibility by replacing linear autoregression with nonlinear fits, they typically fail to exploit known structural properties of the underlying dynamics. In contrast, GGC is specifically designed for ROMs derived from Navier–Stokes equations. By explicitly embedding this physical structure into the regression model, GGC avoids over-parametrisation and ensures the interpretability aligned with the true dynamics. Furthermore, for non-Granger causality methods, we would especially mention the transfer entropy (Schreiber 2000) method, which is theoretically equivalent to Granger causality for Gaussian systems (Barnett, Barrett & Seth 2009) and has been successfully applied to fluid systems (Lozano-Durán *et al.* 2020; Wang *et al.* 2022; Martínez-Sánchez *et al.* 2023; Massaro, Rezaeiravesh & Schlatter 2023). Generally speaking, transfer entropy is a universal, model-free method with a robust theoretical foundation, demonstrating broader applicability than GGC. However, it relies on the estimation of probability densities, which becomes computationally expensive when encountered with high-dimensional systems (Duan *et al.* 2013) and statistically unreliable when data are limited (Smirnov 2013). In contrast, GGC is specifically tailored for Galerkin-structured ROMs. It enables reliable causal inference at low computational cost, thereby demonstrating a distinct advantage over transfer entropy in the context of this study.

The causal structure of the shear flow model has also been investigated in recent works using different causal analysis approaches. For instance, Martínez-Sánchez *et al.* (2023) applied transfer entropy, Lopez-Doriga *et al.* (2024) employed nonlinear Granger causality, while Zhang *et al.* (2024) used a Liang–Kleeman information flow. As shown in figure 19, these methods recover partial causal links but differ in details due to their distinct underlying assumptions. The main contributions of the present paper, compared with previous works, are threefold: (i) data-driven GGC and equation-based analysis are combined to identify causal relations in the shear flow model, resulting in robust,

https://doi.org/10.1017/jfm.2026.11553 Published online by Cambridge University Press

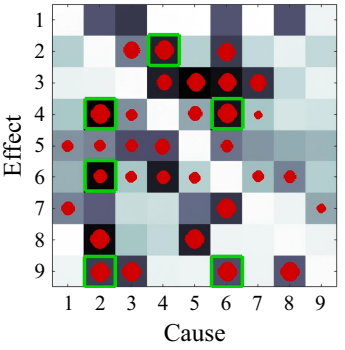


Figure 19. Comparison of various causal analysis methods applied to the shear flow model. The background illustrates results of the GGC. Six significant causal effects, identified by transfer entropy, are marked in green boxes. The causalities uncovered by nonlinear Granger causality are represented by brown circles, with their strength indicated by the size.

reliable cause-and-effect analysis; (ii) mode interactions are identified by the proposed causal analysis, enhancing the physical interpretations of the underlying mechanisms; and (iii) a causality-guided flow control is presented in this model, through applying control body force to the modulating mode (i.e. the modulator). This type of control successfully suppresses extreme events in the shear flow. Together, these contributions connect equation-based understanding, data-driven causal discovery and flow control, offering guidance for more complex flow problems in future work.

6. Conclusions

In this work, we performed causal analysis of a turbulent shear flow developed by Moehlis *et al.* (2004). The analysis helps to characterise nonlinear modal interactions from low-dimensional Galerkin equations and modified Granger causality, named as GGC. The identified two types of quadratic interactions, including a fully triad interaction and a modulated two-mode coupling, as well as the directed cause-and-effect network, offer a causal perspective on the nonlinear flow dynamics and guide the design of flow control strategy.

The proposed GGC is designed for systems following Galerkin-structured dynamics (flow ROMs). It takes modal coefficients as input to formulate a quadratic regression framework and outputs the difference between the prediction with and without the causal mode. Using the GGC, once a mode with large effect is identified, the uncertainties corresponding to the cause mode cannot be ignored. The resulting Granger causal map not only quantifies the cause-and-effect relationships between modes, but also helps identify the quadratic interactions from the equation-based analysis, when transferred to the binary causal map. To assess the applicability of GGC beyond systems with known Galerkin structure, we further apply it to a turbulent lid-driven cavity flow (see Appendix B). Without requiring a pre-existing model, GGC obtains a robust and physically interpretable causal network for the data-driven POD modes. We also show that truncating the system does not significantly alter the inferred causality. These results support GGC as a fully data-driven procedure that allows automated quantification of modal causality.

The proposed causal analysis framework also results in valuable tools for Galerkin modelling, opening promising possibilities in applications of various problems: (i) causal insights may inform reduced-order representation and model-order reduction of nonlinear dynamics (Lassila *et al.* 2014), or developing improved turbulence closures (Shan & Zhang 2025); (ii) sensitivity and uncertainty quantification in modal space, potentially offering a

https://doi.org/10.1017/jfm.2026.11553 Published online by Cambridge University Press

variational perspective related to Lyapunov exponents (Oseledec 1968); and (iii) discovery of the prediction horizon and active subspaces for control design (Bagheri *et al.* 2009). These aspects will be explored in future works.

Supplementary material. Supplementary material is available at https://doi.org/10.1017/jfm.2026.11553.

Funding. This work was supported by the National Key Research and Development Program of China (2024YFB3310401), the Foundation of National Key Laboratory of Aircraft Configuration Design (JBGS-202,504), the Natural Science Foundation of Shaanxi Province (2025JC-YBQN-087), Science and Technology Plan Project of Shaanxi Province (Grant No. 2024JC-YBQN-0010) and the Fundamental Research Funds for the Central Universities (G2024KY05101).

Declaration of interests. The authors report no conflict of interest.

Data availability statement. The codes and datasets used in this study are available in the following repository: https://github.com/JiaqingKou/Galerkin-based-Granger-Causality.

Appendix A. Mode definition of the turbulent shear flow model

The physical domain of turbulent shear flow is set to $0 \leqslant x \leqslant L_x$, $-1 \leqslant y \leqslant 1$, $0 \leqslant z \leqslant L_z$. Let $\alpha = 2\pi/L_x$, $\beta = \pi/2$ and $\gamma = 2\pi/L_z$. Then the velocity in the turbulent shear flow model (Moehlis *et al.* 2004) is projected onto nine Fourier bases (modes), as described below.

The basic profile (shear flow):

$$\boldsymbol{u}_1 = \begin{pmatrix} \sqrt{2}\sin(\pi y/2) \\ 0 \\ 0 \end{pmatrix}. \tag{A1}$$

The streak:

$$\boldsymbol{u}_2 = \begin{pmatrix} \dfrac{4}{\sqrt{3}}\cos^2(\pi y/2)\cos(\gamma z) \\ 0 \\ 0 \end{pmatrix}, \tag{A2}$$

The downstream vortex:

$$\boldsymbol{u}_3 = \frac{2}{\sqrt{4\gamma^2+\pi^2}} \begin{pmatrix} 0 \\ 2\gamma\cos(\pi y/2)\cos(\gamma z) \\ \pi\sin(\pi y/2)\sin(\gamma z) \end{pmatrix}. \tag{A3}$$

The spanwise flows:

$$\boldsymbol{u}_4 = \begin{pmatrix} 0 \\ 0 \\ \dfrac{4}{\sqrt{3}}\cos(\alpha x)\cos^2(\pi y/2) \end{pmatrix} \tag{A4}$$

and

$$\boldsymbol{u}_5 = \begin{pmatrix} 0 \\ 0 \\ 2\sin(\alpha x)\sin(\pi y/2) \end{pmatrix}. \tag{A5}$$

https://doi.org/10.1017/jfm.2026.11553 Published online by Cambridge University Press

The normal vortex modes:

$$\boldsymbol{u}_6 = \frac{4\sqrt{2}}{\sqrt{3(\alpha^2+\gamma^2)}} \begin{pmatrix} -\gamma \cos(\alpha x)\cos^2(\pi y/2)\sin(\gamma z) \\ 0 \\ \alpha \sin(\alpha x)\cos^2(\pi y/2)\cos(\gamma z) \end{pmatrix} \tag{A6}$$

and

$$\boldsymbol{u}_7 = \frac{2\sqrt{2}}{\sqrt{\alpha^2+\gamma^2}} \begin{pmatrix} \gamma \sin(\alpha x)\sin(\pi y/2)\sin(\gamma z) \\ 0 \\ \alpha \cos(\alpha x)\sin(\pi y/2)\cos(\gamma z) \end{pmatrix}. \tag{A7}$$

The fully three-dimensional mode:

$$\boldsymbol{u}_8 = \frac{2\sqrt{2}}{\sqrt{(\alpha^2+\gamma^2)(4\alpha^2+4\gamma^2+\pi^2)}} \begin{pmatrix} \pi\alpha \sin(\alpha x)\sin(\pi y/2)\sin(\gamma z) \\ 2(\alpha^2+\gamma^2)\cos(\alpha x)\cos(\pi y/2)\sin(\gamma z) \\ -\pi\gamma \cos(\alpha x)\sin(\pi y/2)\cos(\gamma z) \end{pmatrix}. \tag{A8}$$

The modification of the basic profile, which is the variation from the eight-mode shear flow model proposed by Waleffe (1997):

$$\boldsymbol{u}_9 = \begin{pmatrix} \sqrt{2}\sin(3\pi y/2) \\ 0 \\ 0 \end{pmatrix}. \tag{A9}$$

Appendix B. Extending GGC to complex problems exemplified by a cavity flow

The proposed GGC framework can be applied to dimensionality reduction techniques (e.g. POD, dynamic mode decomposition or variational autoencoder (Solera-Rico *et al.* 2024)) to enable causal analysis in complex high-dimensional flows. Mathematically, this combination yields a truncated Galerkin system, where the dynamics of the low-dimensional mode coefficients is resolved while higher-order dynamics is excluded. In this reduced-order context, GGC can still recover the underlying causal mechanisms governing the flow dynamics, provided that the truncation error is negligible.

To demonstrate this, the two-dimensional post-transient cavity flow data released by Arbabi & Mezić (2017) are further studied. The flow data are obtained through a Chebyshev spectral collocation simulation of an incompressible lid-driven cavity flow in a square domain $[-1, 1]$. The Reynolds number is defined as $Re = L_c U_c/\nu = 2/\nu$, where $L_c = 2$ and $U_c = 1$ are the characteristic length and velocity, respectively. Previous studies report that the flow is periodic at $Re = 13\,000$, undergoes a Hopf bifurcation and becomes quasi-periodic at $Re = 15\,000$, and transitions to chaos for $Re > 22\,000$. More details about this simulation can be found in the literature (Arbabi & Mezić 2017; Arbabi & Mezic 2019).

We apply the GGC method to the cavity flow at $Re = 16\,000$ (figure 20), using the 64×64 Chebyshev-grid simulation data from Arbabi & Mezić (2017). A POD decomposition is first conducted on a dataset comprising 10^4 velocity snapshots with a time interval of 0.1. For the two-component velocity field, POD is applied to the vector field by concatenating the u- and v-velocity components into a unified snapshot matrix. The first 10 modes take up 71 % of the total energy, capturing the dominant structures of the flow. The resulting POD modes and coefficients are shown in figure 21. A fast Fourier transformation is also conducted on the mode coefficients, which shows that modes 1–4 are dominated by

https://doi.org/10.1017/jfm.2026.11553 Published online by Cambridge University Press

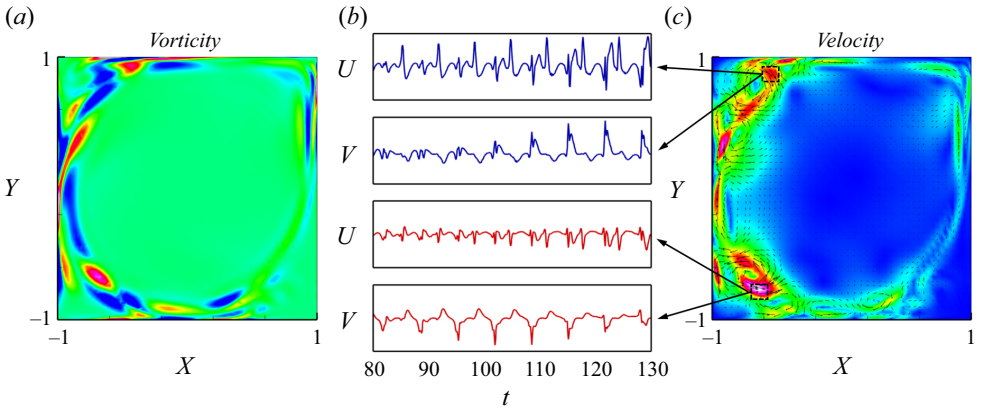


Figure 20. Snapshot of the lid-driven cavity flow at $Re = 16\,000$: (*a*) vorticity field, (*c*) velocity magnitude with superimposed vector field and (*b*) time histories of the velocity components at two selected grid points.

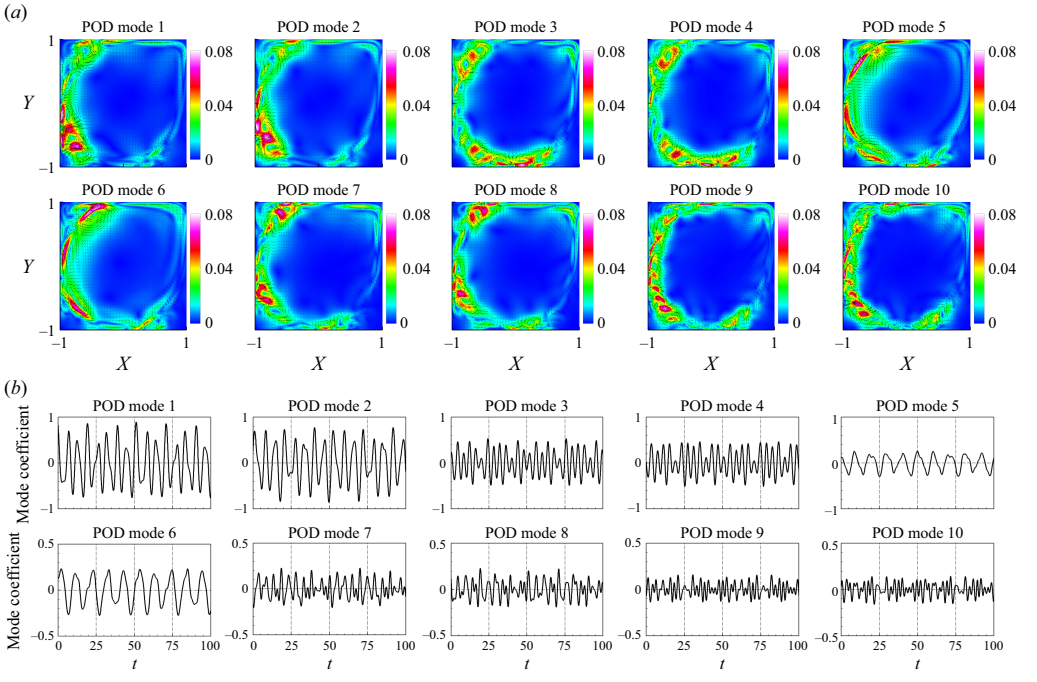


Figure 21. (*a*) Contours of the first 10 velocity POD modes for the lid-driven cavity flow at $Re = 16\,000$, with colour indicating velocity magnitude and black arrows depicting the velocity vectors. (*b*) The temporal coefficients of the first 10 POD modes.

frequencies $St = 0.155$ and $St = 0.252$, modes 5–6 are dominated by a single frequency $St = 0.097$, while modes 7–10 exhibit a mixture of frequencies at $St = 0.194$, $St = 0.349$ and $St = 0.408$. The basic frequency vector of the cavity flow at $Re = 16\,000$ is reported as $St = [0.155, 0.097]$ (Arbabi & Mezić 2017), while the dominant frequencies of the first 10 POD modes are linear combinations of those two basic flow frequencies.

The GGC is then applied to infer causal relationships between the first 10 POD modes. To determine the window length, a variety of window lengths are tested, where the

https://doi.org/10.1017/jfm.2026.11553 Published online by Cambridge University Press

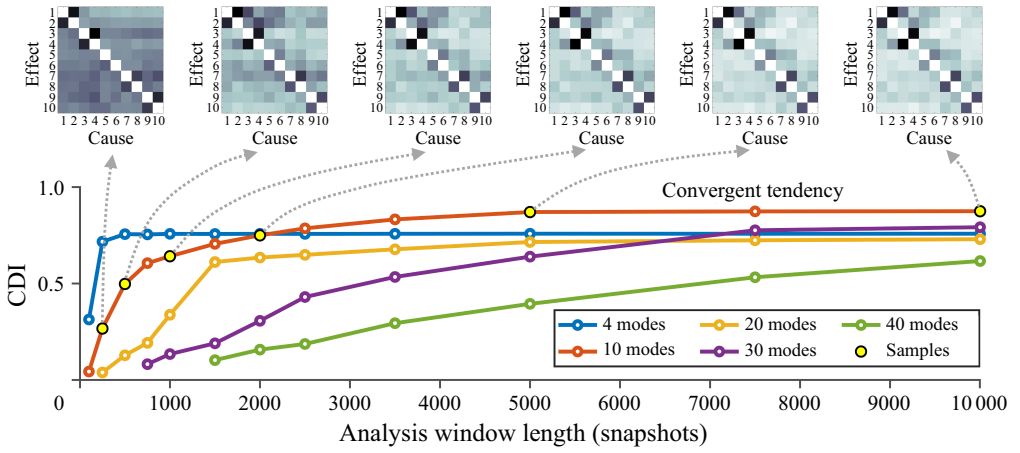


Figure 22. Convergence of the CDI as a function of analysis window length (in snapshots) for GGC analyses using the first 4, 10, 20, 30 and 40 POD modes. In the case of 10 modes, the outcome stabilises beyond 5000 snapshots ($T = 500$). This convergence becomes slower as the number of modes increases, indicating a need for longer windows in higher-dimensional analyses.

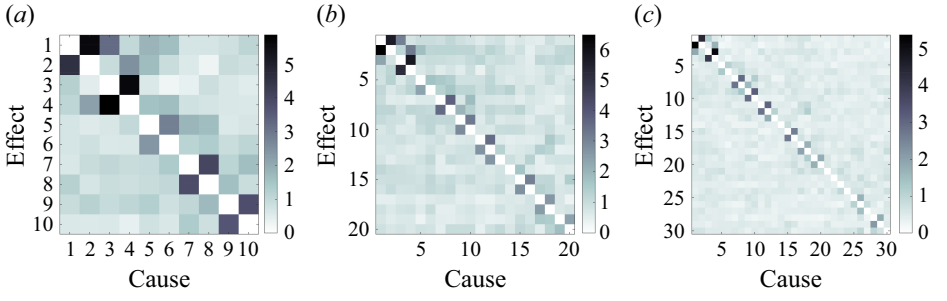


Figure 23. The GGC maps computed using models constructed from (*a*) 10, (*b*) 20 and (*c*) 30 modes. The consistent causal structure of dominant modes across all cases indicates that the results are robust to the inclusion of higher-order modes, supporting the use of GGC on reduced-order systems.

corresponding GGC results and CDI values are shown in figure 22. Similar to the shear flow model, the GGC result and CDI value converge as analysis window length increases, and are stabilised beyond 5000 snapshots ($T = 500$). This determines an optimal window length of 5000 snapshots, which gives a clear causal structure in figure 22. Furthermore, this convergence behaviour is robust across different numbers of modes considered. A key observation is that the window length required for GGC convergence scales with the number of modes, implying that more data are needed to reliably estimate causality in higher-dimensional systems. Permutation test (introduced in § 4) indicates that statistically significant causalities exist among almost all modes. This is reasonable since they are indeed highly coupled. Notably, the strongest causal links occur between conjugate mode pairs (e.g. modes $1 \rightleftharpoons 2$, $3 \rightleftharpoons 4$, etc.).

One of the key assumptions underlying Granger causality is a fully observed system, which requires no unmeasured confounders (Shojaie & Fox 2022). Since GGC is essentially a Granger causality test applied to a low-dimensional Galerkin model, a natural concern is whether truncating the model by excluding higher-order POD modes may bias the causal inference. To address this, we performed sensitivity analyses on models

https://doi.org/10.1017/jfm.2026.11553 Published online by Cambridge University Press

constructed with varying numbers of POD modes (figure 23). The results reveal that the causal structure among the first 10 modes remains highly consistent across analyses involving 10, 20 and 30 modes. This suggests that the exclusion of higher-order dynamics does not significantly compromise the inferred causal relationships among the dominant modes, which can be attributed to the localised nature of the dynamics. As figure 23 clearly illustrates, strong causal links only exist between neighbouring modes, while the couplings between lower-order and higher-order modes are weak or negligible. However, this approximation may not hold for all flow configurations. For cases where outcomes are sensitive to mode truncation, potential solutions include increasing the number of modes preserved, or extending the GGC framework with higher-order nonlinearity to model the effect of truncated modes (Noack *et al.* 2003; Loiseau & Brunton 2018).

A GGC analysis to the cavity flow at $Re = 30,000$ is further provided in the supplementary material. These support the validity of GGC on more complicated flow problems. A deep physical interpretation of the above causal observations lies beyond the scope of the present work, while future works may investigate the underlying mechanisms of these results.

References

Akhtar, I. 2008 Parallel simulations, reduced-order modeling, and feedback control of vortex shedding using fluidic actuators.

Ancona, N., Marinazzo, D. & Stramaglia, S. 2004 Radial basis function approach to nonlinear Granger causality of time series. *Phys. Rev. E—Stat. Nonlinear Soft Matt. Phys.* **70** (5), 056221.

Andrzejak, R.G., Kraskov, A., Stögbauer, H., Mormann, F. & Kreuz, T. 2003 Bivariate surrogate techniques: necessity, strengths, and caveats. *Phys. Rev. E* **68** (6), 066202.

Arbabi, H. & Mezić, I. 2017 Study of dynamics in post-transient flows using Koopman mode decomposition. *Phys. Rev. Fluids* **2** (12), 124402.

Arbabi, H. & Mezic, I. 2019 Spectral analysis of mixing in 2D high-Reynolds flows. arXiv preprint arXiv:1903.

Bagchi, S., Unni, V.R. & Saha, A. 2023 Transition to limit-cycle oscillation in fluid-structure interactions: mutual correlations and causal dependencies. *AIAA J.* **61** (4), 1475–1484.

Bagheri, S., Henningson, D.S., Hœpffner, J. & Schmid, P.J. 2009 Input–output analysis and control design applied to a linear model of spatially developing flows. *Appl. Mech. Rev.* **62** (2), 020803.

Balajewicz, M.J., Dowell, E.H. & Noack, B.R. 2013 Low-dimensional modelling of high-Reynolds-number shear flows incorporating constraints from the Navier–Stokes equation. *J. Fluid Mech.* **729**, 285–308.

Barnett, L., Barrett, A.B. & Seth, A.K. 2009 Granger causality and transfer entropy are equivalent for Gaussian variables. *Phys. Rev. Lett.* **103** (23), 238701.

Barnett, L. & Seth, A.K. 2014 The MVGC multivariate Granger causality toolbox: a new approach to Granger-causal inference. *J. Neuroscience Meth.* **223**, 50–68.

Borgonovo, E. & Plischke, E. 2016 Sensitivity analysis: a review of recent advances. *Eur. J. Oper. Res.* **248** (3), 869–887.

Brunton, S.L., Noack, B.R. & Koumoutsakos, P. 2020 Machine learning for fluid mechanics. *Annu. Rev. Fluid Mech.* **52** (1), 477–508.

Brunton, S.L., Proctor, J.L. & Kutz, J.N. 2016 Discovering governing equations from data by sparse identification of nonlinear dynamical systems. *Proc. Natl Acad. Sci. USA* **113** (15), 3932–3937.

Bryson, A.E. 2018 *Applied Optimal Control: Optimization, Estimation and Control*. Routledge.

Camps-Valls, G., Gerhardus, A., Ninad, U., Varando, G., Martius, G., Balaguer-Ballester, E., Vinuesa, R., Diaz, E., Zanna, L. & Runge, J. 2023 Discovering causal relations and equations from data. *Phys. Rep.* **1044**, 1–68.

Chen, K.K., Tu, J.H. & Rowley, C.W. 2012 Variants of dynamic mode decomposition: boundary condition, Koopman, and Fourier analyses. *J. Nonlinear Sci.* **22** (6), 887–915.

Cremades, A. *et al.* 2024 Identifying regions of importance in wall-bounded turbulence through explainable deep learning. *Nat. Commun.* **15** (1), 3864.

Cremades, A., Hoyas, S. & Vinuesa, R. 2025 Classically studied coherent structures only paint a partial picture of wall-bounded turbulence. *Nat. Commun.* **16** (1), 10189.

https://doi.org/10.1017/jfm.2026.11553 Published online by Cambridge University Press

DEANE, A.E., KEVREKIDIS, I.G., KARNIADAKIS, G.E. & ORSZAG, S.A. 1991 Low-dimensional models for complex geometry flows: application to grooved channels and circular cylinders. *Phys. Fluids A: Fluid Dyn.* **3** (10), 2337–2354.

DING, M., CHEN, Y. & BRESSLER, S.L. 2006 Granger causality: basic theory and application to neuroscience. In *Handbook of Time Series Analysis: Recent Theoretical Developments and Applications*, pp. 437–460. Wiley Online Library.

DUAN, P., YANG, F., CHEN, T. & SHAH, S.L. 2013 Direct causality detection via the transfer entropy approach. *IEEE Trans. Control Syst. Technol.* **21** (6), 2052–2066.

ENCINAR, M.P. & JIMÉNEZ, J. 2023 Identifying causally significant features in three-dimensional isotropic turbulence. *J. Fluid Mech.* **965**, A20.

FREEMAN, J.R. 1983 Granger causality and the times series analysis of political relationships. *Am. J. Political Sci.* **27** (2), 327–358.

GALLETTI, B., BRUNEAU, C.H., ZANNETTI, L. & IOLLO, A. 2004 Low-order modelling of laminar flow regimes past a confined square cylinder. *J. Fluid Mech.* **503**, 161–170.

GRANGER, C.W.J. 1969 Investigating causal relations by econometric models and cross-spectral methods. *Econometrica: J. Econometric Soc.* **37** (3), 424–438.

GUASTONI, L., GÜEMES, A., IANIRO, A., DISCETTI, S., SCHLATTER, P., AZIZPOUR, H. & VINUESA, R. 2021 Convolutional-network models to predict wall-bounded turbulence from wall quantities. *J. Fluid Mech.* **928**, A27.

HIEMSTRA, C. & JONES, J.D. 1994 Testing for linear and nonlinear granger causality in the stock price-volume relation. *J. Finance* **49** (5), 1639–1664.

HOLMES, P. 2012 *Turbulence, Coherent Structures, Dynamical Systems and Symmetry*. Cambridge University Press.

IOLLO, A., LANTERI, S. & DÉSIDÉRI, J.-A. 2000 Stability properties of POD–Galerkin approximations for the compressible Navier–Stokes equations. *Theor. Comput. Fluid Dyn.* **13** (6), 377–396.

JIMÉNEZ, J. 2018 Machine-aided turbulence theory. *J. Fluid Mech.* **854**, R1.

JOHANSEN, S. 1988 Statistical analysis of cointegration vectors. *J. Economic Dyn. Control* **12** (2–3), 231–254.

KAISER, E., NOACK, B.R., CORDIER, L., SPOHN, A., SEGOND, M., ABEL, M., DAVILLER, G., ÖSTH, J., KRAJNOVIĆ, S. & NIVEN, R.K. 2014 Cluster-based reduced-order modelling of a mixing layer. *J. Fluid Mech.* **754**, 365–414.

KRAICHNAN, R.H. & CHEN, S. 1989 Is there a statistical mechanics of turbulence? *Phys. D: Nonlinear Phenom.* **37** (1–3), 160–172.

LASSILA, T., MANZONI, A., QUARTERONI, A. & ROZZA, G. 2014 Model order reduction in fluid dynamics: challenges and perspectives. In *Reduced Order Methods for Modeling and Computational Reduction*, pp. 235–273. Springer.

LE CLAINCHE, S. & VEGA, J. 2017 Higher order dynamic mode decomposition. *SIAM J. Appl. Dyn. Syst.* **16** (2), 882–925.

LOISEAU, J.-C. & BRUNTON, S.L. 2018 Constrained sparse Galerkin regression. *J. Fluid Mech.* **838**, 42–67.

LOISEAU, J.-C., NOACK, B.R. & BRUNTON, S.L. 2018 Sparse reduced-order modelling: sensor-based dynamics to full-state estimation. *J. Fluid Mech.* **844**, 459–490.

LOPEZ-DORIGA, B., ATZORI, M., VINUESA, R., BAE, H.J., SRIVASTAVA, A. & DAWSON, S.T.M. 2024 Linear and nonlinear granger causality analysis of turbulent duct flows. *J. Phys.: Conf. Ser.* **2753**, 012017.

LOZANO-DURÁN, A. & ARRANZ, G. 2022 Information-theoretic formulation of dynamical systems: causality, modeling, and control. *Phys. Rev. Res.* **4** (2), 023195.

LOZANO-DURÁN, A., BAE, H.J. & ENCINAR, M.P. 2020 Causality of energy-containing eddies in wall turbulence. *J. Fluid Mech.* **882**, A2.

LOZANO-DURÁN, A., CONSTANTINOU, N.C., NIKOLAIDIS, M.-A. & KARP, M. 2021 Cause-and-effect of linear mechanisms sustaining wall turbulence. *J. Fluid Mech.* **914**, A8.

LUMLEY, J.L. 1967 The structure of inhomogeneous turbulent flows. In *Atmospheric Turbulence and Radio Wave Propagation*, pp. 166–178. Nauka.

MARINAZZO, D., PELLICORO, M. & STRAMAGLIA, S. 2008 Kernel-Granger causality and the analysis of dynamical networks. *Phys. Rev. E—Stat. Nonlinear Soft Matt. Phys.* **77** (5), 056215.

MARTÍNEZ-SÁNCHEZ, Á., ARRANZ, G. & LOZANO-DURÁN, A. 2024 Decomposing causality into its synergistic, unique, and redundant components. *Nat. Commun.* **15** (1), 9296.

MARTÍNEZ-SÁNCHEZ, Á., LÓPEZ, E., LE CLAINCHE, S., LOZANO-DURÁN, A., SRIVASTAVA, A. & VINUESA, R. 2023 Causality analysis of large-scale structures in the flow around a wall-mounted square cylinder. *J. Fluid Mech.* **967**, A1.

MARTÍNEZ-SÁNCHEZ, Á. & LOZANO-DURÁN, A. 2025 Observational causality by states and interaction type for scientific discovery. *Commun. Phys.* **9** (1), 15.

https://doi.org/10.1017/jfm.2026.11553 Published online by Cambridge University Press

MASSARO, D., REZAEIRAVESH, S. & SCHLATTER, P. 2023 On the potential of transfer entropy in turbulent dynamical systems. *Sci. Rep. UK* **13** (1), 22344.
MENDEZ, M.A., BALABANE, M. & BUCHLIN, J.-M. 2019 Multi-scale proper orthogonal decomposition of complex fluid flows. *J. Fluid Mech.* **870**, 988–1036.
MOEHLIS, J., FAISST, H. & ECKHARDT, B. 2004 A low-dimensional model for turbulent shear flows. *New J. Phys.* **6** (1), 56.
MURATA, T., FUKAMI, K. & FUKAGATA, K. 2020 Nonlinear mode decomposition with convolutional neural networks for fluid dynamics. *J. Fluid Mech.* **882**, A13.
NOACK, B.R., AFANASIEV, K., MORZYŃSKI, M., TADMOR, G. & THIELE, F. 2003 A hierarchy of low-dimensional models for the transient and post-transient cylinder wake. *J. Fluid Mech.* **497**, 335–363.
NOACK, B.R., PAPAS, P. & MONKEWITZ, P.A. 2005 The need for a pressure-term representation in empirical Galerkin models of incompressible shear flows. *J. Fluid Mech.* **523**, 339–365.
NOACK, B.R., SCHLEGEL, M., AHLBORN, B., MUTSCHKE, G., MORZYŃSKI, M., COMTE, P. & TADMOR, G. 2008 A finite-time thermodynamics of unsteady fluid flows. *J. Non-Equilib. Thermodyn.* **33** (2), 103–148.
NOACK, B.R., STANKIEWICZ, W., MORZYŃSKI, M. & SCHMID, P.J. 2016 Recursive dynamic mode decomposition of transient and post-transient wake flows. *J. Fluid Mech.* **809**, 843–872.
OMATA, N. & TSUTSUMI, S. 2020 Causal analysis of flowfields using clustering entropy. *AIAA J.* **58** (12), 5472–5477.
OSELEDEC, V.I. 1968 A multiplicative ergodic theorem, Lyapunov characteristic numbers for dynamical systems. *Trans. Moscow Math. Soc.* **19**, 197–231.
ÖSTH, J., NOACK, B.R., KRAJNOVIĆ, S., BARROS, D. & BORÉE, J. 2014 On the need for a nonlinear subscale turbulence term in POD models as exemplified for a high-Reynolds-number flow over an Ahmed body. *J. Fluid Mech.* **747**, 518–544.
QUIAN QUIROGA, R., KRASKOV, A., KREUZ, T. & GRASSBERGER, P. 2002 Performance of different synchronization measures in real data: a case study on electroencephalographic signals. *Phys. Rev. E* **65** (4), 041903.
RACCA, A. & MAGRI, L. 2022 Data-driven prediction and control of extreme events in a chaotic flow. *Phys. Rev. Fluids* **7** (10), 104402.
REMPFER, D. 2000 On low-dimensional Galerkin models for fluid flow. *Theor. Comput. Fluid Dyn.* **14** (2), 75–88.
RIGAS, G., OXLADE, A.R., MORGANS, A.S. & MORRISON, J.F. 2014 Low-dimensional dynamics of a turbulent axisymmetric wake. *J. Fluid Mech.* **755**, R5.
ROWLEY, C.W., COLONIUS, T. & MURRAY, R.M. 2004 Model reduction for compressible flows using POD and Galerkin projection. *Phys. D: Nonlinear Phenom.* **189** (1–2), 115–129.
ROWLEY, C.W. & DAWSON, S.T.M. 2017 Model reduction for flow analysis and control. *Annu. Rev. Fluid Mech.* **49** (1), 387–417.
ROWLEY, C.W., MEZIĆ, I., BAGHERI, S., SCHLATTER, P. & HENNINGSON, D.S. 2009 Spectral analysis of nonlinear flows. *J. Fluid Mech.* **641**, 115–127.
SAFIKHANI, A. & SHOJAIE, A. 2022 Joint structural break detection and parameter estimation in high-dimensional nonstationary VAR models. *J. Am. Stat. Assoc.* **117** (537), 251–264.
SAPSIS, T.P. 2021 Statistics of extreme events in fluid flows and waves. *Annu. Rev. Fluid Mech.* **53** (1), 85–111.
SCHMID, P.J. 2010 Dynamic mode decomposition of numerical and experimental data. *J. Fluid Mech.* **656**, 5–28.
SCHREIBER, T. 2000 Measuring information transfer. *Phys. Rev. Lett.* **85** (2), 461.
SHAN, X.L. & ZHANG, W.W. 2025 Data-driven adverse pressure gradient correction for turbulence model. *AIAA J.* **63** (7), 2780–2796.
SHOJAIE, A. & FOX, E.B. 2022 Granger causality: a review and recent advances. *Annu. Rev. Stat. Applics* **9** (1), 289–319.
SIROVICH, L. 1987 Turbulence and the dynamics of coherent structures: I. Coherent structures. *Q. Appl. Maths* **45** (3), 561–571.
SKUFCA, J.D., YORKE, J.A. & ECKHARDT, B. 2006 Edge of chaos in a parallel shear flow. *Phys. Rev. Lett.* **96** (17), 174101.
SMIRNOV, D.A. 2013 Spurious causalities with transfer entropy. *Phys. Rev. E—Stat. Nonlinear Soft Matt. Phys.* **87** (4), 042917.
SMIRNOV, D.A. & MOKHOV, I.I. 2009 From granger causality to long-term causality: application to climatic data. *Phys. Rev. E—Stat. Nonlinear Soft Matt. Phys.* **80** (1), 016208.

https://doi.org/10.1017/jfm.2026.11553 Published online by Cambridge University Press

SOLERA-RICO, A., SANMIGUEL VILA, C., GÓMEZ-LÓPEZ, M., WANG, Y., ALMASHJARY, A., DAWSON, S.T.M. & VINUESA, R. 2024 β-variational autoencoders and transformers for reduced-order modelling of fluid flows. *Nat. Commun.* **15** (1), 1361.

SRINIVASAN, P.A., GUASTONI, L., AZIZPOUR, H., SCHLATTER, P.H.I.L.I.P.P. & VINUESA, R. 2019 Predictions of turbulent shear flows using deep neural networks. *Phys. Rev. Fluids* **4** (5), 054603.

STOKES, P.A. & PURDON, P.L. 2017 A study of problems encountered in Granger causality analysis from a neuroscience perspective. *Proc. Natl Acad. Sci. USA* **114** (34), E7063–E7072.

TANK, A., COVERT, I., FOTI, N., SHOJAIE, A. & FOX, E.B. 2021 Neural Granger causality. *IEEE Trans. Pattern Anal. Mach. Intell.* **44** (8), 4267–4279.

TISSOT, G., LOZANO-DURÁN, A., CORDIER, L., JIMÉNEZ, J. & NOACK, B.R. 2014 Granger causality in wall-bounded turbulence. *J. Phys.: Conf. Ser.* **506**, 012006.

TONONI, G. & SPORNS, O. 2003 Measuring information integration. *BMC Neuroscience* **4**, 1–20.

TOWNE, A., SCHMIDT, O.T. & COLONIUS, T. 2018 Spectral proper orthogonal decomposition and its relationship to dynamic mode decomposition and resolvent analysis. *J. Fluid Mech.* **847**, 821–867.

WALEFFE, F. 1997 On a self-sustaining process in shear flows. *Phys. Fluids* **9** (4), 883–900.

WANG, W., CHU, X., LOZANO-DURÁN, A., HELMIG, R. & WEIGAND, B. 2021 Information transfer between turbulent boundary layers and porous media. *J. Fluid Mech.* **920**, A21.

WANG, W., LOZANO-DURAN, A., HELMIG, R. & CHU, X. 2022 Spatial and spectral characteristics of information flux between turbulent boundary layers and porous media. *J. Fluid Mech.* **949**, A16.

WIENER, N. 1949 *Extrapolation, Interpolation, and Smoothing of Stationary Time Series: with Engineering Applications*. The MIT press.

ZHANG, J., ZHU, Z., VINUESA, R. & HU, R. 2024 Causal analysis of inner and outer motions in near-wall turbulent flow. arXiv preprint arXiv:2404.08907.

ZHANG, P., ROSEN, M., PETERSON, S.D. & PORFIRI, M. 2018 An information-theoretic approach to study fluid–structure interactions. *J. Fluid Mech.* **848**, 968–986.

https://doi.org/10.1017/jfm.2026.11553 Published online by Cambridge University Press